Val, P., Hoke, G. D., Fosdick, J. C., Wittmann, H. (2016): Reconciling tectonic shortening, sedimentation and spatial patterns of erosion from 10Be paleo-erosion rates in the Argentine Precordillera. - *Earth and Planetary Science Letters*, *450*, pp. 173–185.

DOI: http://doi.org/10.1016/j.epsl.2016.06.015

Reconciling tectonic shortening, sedimentation and spatial patterns of erosion from ^{10}Be paleo-erosion rates in the Argentine Precordillera

Pedro Val[a*]; Gregory D. Hoke[a]

[a]*Dept. of Earth Sciences, Syracuse University, 204 Heroy Geology Lab., Syracuse NY, USA 13244*

Julie C. Fosdick[b]

[b]*Dept. of Geological Sciences, Indiana University, 1001 East 10[th] Street, Bloomington, IN, USA 47405*

Hella Wittmann[c]

[c]*Helmholtz Centre Potsdam, GFZ German Research Center for Geosciences, Telegrafenberg E 228, 14473 Potsdam, Germany*

Correspondence and request for supplementary material to:
P. Val,
pfval@syr.edu

Highlights

- Paleo-erosion rates were extracted from the 7.7 – 1.8 Ma sedimentary rocks
- Spatial control of erosion reveals upstream migration of an erosion wave
- Peak catchment-wide erosion lags shortening pulse by ~2 Ma

Abstract

The temporal evolution of erosion over million-year timescales is key to understand the development of mountain ranges and adjacent fold-and-thrust belts. While models of orogenic wedge dynamics predict an instantaneous response of erosion to pulses of rock uplift, stream-power based models predict that catchment-wide erosion maxima significantly lag behind a pulse of rock uplift. Here, we explore the relationships between rock uplift, erosion, and sediment deposition in the Argentine Precordillera fold-and-thrust belt at 30°S. Using a combination of ^{10}Be-derived paleo-erosion rates, constraints on re-exposure using ^{26}Al/^{10}Be ratios, geomorphic observations and detrital zircon provenance, we demonstrate that the attainment of maximum upland erosion rates lags the maximum rate of deformation over million-year timescales. The magnitudes and causes of the erosional delays shed new light on the catchment erosional response to tectonic deformation and rock uplift in orogenic wedges.

Keywords

^{10}Be paleo-erosion rates, rock uplift, compressional mountain range, time-lag, detrital zircon provenance; Andes

1. Introduction

Temporal variations of erosion rates should be diagnostic of whether tectonic or climatic processes govern mass fluxes in and out of orogens (e.g. Whipple, 2009). Sediment accumulation rates derived from magnetostratigraphy provide important clues about those mass fluxes, but are often insufficient for completing mass balances (i.e. linking erosion to deposition). For example, magnetostratigraphy only allows calculation of upland erosion rates if a basin is underfilled. Otherwise, the best inference is that sediment supply keeps pace with or exceeds the rate of creation of accommodation in the basin. In the latter case, sediment is bypassed beyond the depocenter, thereby hindering mass balance approximations. Therefore, despite routinely providing rates of flexural foreland basin development related to the history of upland deformation (Jordan et al., 1993), sediment accumulation rates are only half of the story. The missing half consists of linking the histories of deformation and sediment accumulation to upland erosion.

The combination of spatial and temporal patterns of wedge-widening or narrowing, near-surface rock uplift rates, erosion and sedimentation rates can reveal the temporal evolution of an orogenic wedge (Whipple, 2009). Numerical and analytical modeling consistently predict abrupt or gradual changes in erosion coeval with rock uplift as diagnostic signs of tectonic or climatic perturbations, respectively (Fig.1a, b; Stolar et al., 2006; Whipple and Meade, 2006). In these models, the coupling between erosion and rock-uplift stems from isostatic compensation as well as the assumed constancy of critical taper angles, which requires commensurate changes in mass fluxes (Fig. 1a, b; Stolar et al., 2006; Whipple and Meade, 2006; Whipple, 2009). This set of diagnostic behaviors can be investigated in foreland basins (Whipple, 2009).

The contrast between landscape response time and the duration of perturbation is also highly important when determining climate *versus* tectonics (Braun et al., 2015; Whipple, 2009). The predicted post-perturbation landscape response times of orogenic wedges are primarily modulated by erosional efficiency, which is in turn governed by bedrock erodibility and precipitation (Stolar et al., 2006; Whipple and Meade, 2006). If response times are fast enough, changes in deformation and erosion in orogenic systems like the Central Andes can be simultaneous (Whipple, 2009). However, the magnitude and timescale of the tectonic perturbation can also govern fluvial response times at the catchment scale due to a primary control of channel gradient on knickpoint propagation (e.g. Kooi and Beaumont, 1996; Whittaker and Boulton, 2012). This relationship is further supported by numerical modeling of catchment-wide ^{10}Be-erosion rates that suggests a time-lag between a change in tectonically driven rock uplift and a corresponding change in catchment-wide erosion rate (Fig. 1c; Willenbring et al., 2013). Thus, for the tectonic end-member, not only may the erosional response be gradual, but also lagged with respect to the tectonic perturbation (Fig. 1b, c).

Time-lags between upland exhumation, erosion and deposition are often observed in low-temperature detrital thermochronology (e.g. Garver et al., 1999). Since detrital thermochronology typically integrates over the upper kilometers of the crust and 10^6 to 10^7 yr timescales, the technique lacks the sensitivity needed to resolve changes in erosion on sub-Ma timescales (Rahl et al., 2007). Alternatively, ^{10}Be-derived erosion rates are much more sensitive to temporal variations in erosion since they average over the uppermost meters of the Earth's surface and integrate erosion over 10^3-10^5 yr. This sensitivity is sufficient to detect changes in erosion rates on timescales shorter than typical time-lags present in detrital thermochronology. In alluvium, measured ^{10}Be concentrations constitute an average of the upstream area, and therefore reflect a mean catchment erosion rate (e.g. Granger et al., 1996). The same concept can be applied to buried sediments of known age and allows estimation of paleo-erosion rates using ^{10}Be alone. For example, when extracted from the stratigraphic record, ^{10}Be concentrations can reveal the history of erosion rates of the adjacent uplands (e.g. Charreau et al., 2011). This can be complemented with a record of the spatial patterns in upland erosion through sediment provenance indicators of unique igneous sources, such as detrital zircon crystallization ages (e.g. Gehrels, 2011). Applied together in connected intermontane and foreland basins, these methods constitute a powerful means for constructing a complete view of the dynamics of tectonics, erosion and deposition in orogenic systems that is sensitive at sub-Ma timescales.

In this study, we combine ^{10}Be paleo-erosion rates and detrital zircon U-Pb geochronologic age distributions from three stratigraphic sections to construct a spatial and temporal view of erosion in the Andean foreland at 30° S from 8-2 Ma (Fig. 2). The period investigated here is marked by increased shortening and rock-uplift rates in the Precordillera fold-and-thrust belt as well as a relatively steady semi-arid climate (Fig. 3, 4). This framework allows the evaluation of the tectonic end-member of an orogenic-wedge's evolution (Fig. 1b). Thus, based on the modeling predictions of the interplay between erosion and tectonics (Fig. 1b, c), we expect to find a gradual and potentially lagged erosional signal with respect to deformation in the Precordillera.

2. History of deformation and sediment accumulation

At 30°S the main tectonic provinces in the Andes are, from west to east, the Principal and Frontal Cordilleras, the Precordillera fold-and-thrust belt and the Sierras Pampeanas (Fig. 2a). Deformation in the Precordillera is well-constrained through the chronostratigraphy of thrust-top synorogenic sediments (Jordan et al., 1993), balanced cross-sections (Allmendinger and Judge, 2014), and low-temperature thermochronology (Fig 3a; Fosdick et al., 2015). Major thrust activity began ca. 19 Ma in the Western Precordillera (Fig. 3a; Jordan et al., 1993). Shortening rates and exhumation peaked ca. 12-9 Ma during simultaneous movement on the Blanco, Blanquitos, and San Roque thrusts (Fig. 3a, b and Fig. 4; Allmendinger and Judge, 2014; Levina et al., 2014). From 8 to 1 Ma, deformation continued on the San Roque thrust and migrated east to the Niquivil thrust (Fig. 3a, 4). Immediately to the east, deformation and exhumation of the Bermejo Basin deposits initiated ca. 3-2 Ma through west-verging blind thrusts forming the Eastern Precordillera (Fig. 3a, 4; Fosdick et al., 2015; Jordan et al., 2001; Zapata and Allmendinger, 1996). Here, we targeted deeply exhumed stratigraphic sections along cores of anticlines that contain, to a first order, the history of erosional unloading of the adjacent tectonic provinces (Fig. 4).

The development of the Precordillera fold-and-thrust belt segmented the foreland into sub-basins (wedge-top and foredeep) early in its history (Beer et al., 1990; Jordan et al., 1993). Out-of-sequence exhumation occurred in the edges of the wedge-top basin ca. 5 Ma and marks the latest detectable unroofing of the Frontal Cordillera and of the Cerro Negro and Tranca thrusts (Fig. 3a, 4; Fosdick et al., 2015). Deformation of the wedge-top deposits continued to occur until at least 300 ka along the El Tigre fault system (Fig. 4b; Siame et al., 1997). Here, we sampled the wedge-top section to obtain a view of mass-fluxes upstream of the wedge in addition to the foreland-N and foreland-S (Fig. 4).

Sediment accumulation rates in the flexural foredeep reflect the pace of tectonic subsidence and/or sediment supply during upland crustal thickening and tectonic shortening in the Precordillera (Fig. 3b, c; Johnson et al., 1986; Jordan et al., 1993). Paleomagnetic data from the section foreland-N indicate two accumulation rate maxima at 8 Ma and 4.5 Ma since ca. 15 Ma (Fig. 3c; Jordan et al., 1993, 2001). At the section foreland-S, accumulation rates peaked ca. 6 Ma and declined until 1.8 Ma (Fig. 3c; Milana et al., 2003). At foreland-S, a major change in sedimentary facies from small, ephemeral drainage system to one with high transport capacity occurred ca. 4 Ma (Milana et al., 2003), coincident with the abandonment of the Río Jáchal of the foreland-N area (Jordan et al., 2001). Meanwhile, in the wedge-top section, the history of sediment accumulation appears uncorrelated with Precordillera thrust activity (Fig. 3c; Ruskin and Jordan, 2007).

Eastward propagation of deformation in the Precordillera is often compared to the critical Coulomb wedge model (e.g. Allmendinger et al., 1990) that balances tectonic and erosional mass fluxes (Dahlen, 1990). In a critical taper that is not at steady state, an increase in crustal shortening may cause the mass flux into the wedge to temporarily outpace erosional mass flux out and steepen the taper angle. However, the steeper taper will tend to increase erosion rates and return the wedge to its critical state. Alternatively, climatically driven erosion will remove mass from the wedge and decrease its taper. This, in turn, triggers renewed, out-of-sequence deformation coeval with a retreat of the deformation front (i.e. wedge narrowing) to reestablish its critical taper. If the Precordillera behaves similarly, we expect erosion highs to accompany wedge-narrowing if they are climate-driven. Conversely, we expect wedge-widening to precede erosional signals if they are tectonically driven.

3. Methods

3.1 Cosmogenic Nuclides

3.1.1 Sampling strategy

We targeted stratigraphic sections in key locations within the orogenic wedge, which allows monitoring of the dynamics of paleo-erosion upstream and downstream of the active Precordillera fold-and-thrust belt (Fig. 4, 5). Location and depositional age data were obtained from previously published paleomagnetic studies in the wedge-top, foreland-N and foreland-S sections (Fig. 3-5). The depositional ages were corrected to the 2012 geologic time scale (Hilgen et al., 2012). We minimized post-burial re-exposure by sampling from the base of overhanging ledges with at least 3 m of rock above the sample wherever possible (Fig. A.1); otherwise, we targeted vertical cliffs with obvious signs of outcrop instability, such as rock fall. Nonetheless, we measured ^{26}Al and ^{10}Be concentrations in three replicate samples (one from each section) to quantify the modern cosmogenic nuclide dose.

3.1.2 Sample preparation

Medium to coarse-grained sandstones were collected from each section. Samples were crushed and sieved to 250-500 μm (n=16), or 150-500 μm (n=2) for samples with low quartz yield, and processed to obtain pure quartz at Syracuse University. Cosmogenic beryllium (^{10}Be) was extracted from quartz separates spiked with a ^{9}Be carrier (372.5 ppm) at the GeoForschungsZentrum (GFZ) following standard methods (von Blanckenburg et al., 1996). $^{10}Be/^{9}Be$ ratios were measured with accelerator mass spectrometry (AMS) at the University of Cologne relative to standards KN01-6-2 ($^{10}Be/^{9}Be$ of 5.35×10^{-13}) and KN01-5-3 ($^{10}Be/^{9}Be$ of 6.32×10^{-12}; Nishiizumi et al., 2007). Procedural blanks yielded a $^{10}Be/^{9}Be$ ratio of $(6.6 \pm 5.4) \times 10^{-16}$. Blank-corrected sample ratios range from 9.9×10^{-15} to 1×10^{-13} (supplementary Table A.1).

^{26}Al and ^{10}Be were measured from separate, newly weighted aliquots of three replicate samples. ^{26}Al was extracted at GFZ following standard methods (Goethals et al., 2009). Total stable ^{27}Al in each sample was measured using inductively coupled optical emission spectrometer (ICP-OES) at GFZ using the 396.152 nm wavelength. No ^{27}Al spike was added to samples. For the procedural blank, we added 2.029 g of 1,000 ppm Merck-Carrier ^{27}Al. $^{26}Al/^{27}Al$ were measured at the Purdue Rare Isotope Measurement

Laboratory (PRIME) relative to standards in Nishiizumi et al. (2004). Raw Al AMS and ICP-OES data are provided in supplementary material (Table A.2). The measured procedural Al blank $^{26}Al/^{27}Al$ ratio is $0.8 \pm 0.4 \times 10^{-15}$, which is well below the measured sample ratios. The replicate $^{10}Be/^{9}Be$ was measured at the University of Cologne and its procedural $^{10}Be/^{9}Be$ blank was $2.23 \times 10^{-15} \pm 29\%$, causing a 15%-30% difference between this and the original measurements. Due to the better blank measurements from the original analysis, we use the ^{10}Be data associated with the lower procedural blank.

3.1.3 ^{10}Be and ^{26}Al production rates

Spallation and muon production rates are scaled using the time-dependent LSD scaling routine implemented in CRONUScalc (Lifton et al., 2014; Marrero et al., 2016). Scaling factors are relative to a sea-level high latitude (SLHL) ^{10}Be and ^{26}Al productions of 4.09 $\pm$ 0.35 at.g^{-1}.a^{-1} and 28.6 $\pm$ 3.3 at.g^{-1}.a^{-1}, respectively (Phillips et al., 2015). For production during aggradation and burial (P_{burial}), the elevations of the paleo-depocenters were assumed to be similar to modern: 800 m at foreland-N, 700 m at foreland-S, and 1,500 m in the wedge-top, all at ~30°S. For modern production during recent exhumation ($P_{outcrop}$), we used sample elevations, latitudes and outcrop geometry (Gosse and Phillips, 2001).

The production rate on the hillslope during erosion ($P_{hillslope}$) is calculated based on the modern elevation of both the Frontal Cordillera and Precordillera ranges (Fig. 2c; see Section 4.1 about paleo-elevations). This is necessary because the physiography of the area is complex and forms multi-modal distributions of elevations that precludes the conventional pixel-by-pixel arithmetic averaging (Fig. 2c). Thus, we fit a Gaussian curve to the hypsometry of each physiographic province to obtain a mean elevation that is independent of changes in the configuration of the catchment while assuming that the main source areas are the mountains (Fig. 2c). Excluding quartz-poor lithologies does not significantly change the hypsometries (Fig. A.2).

Based on detrital zircon provenance data from the literature (see Section 5.4, Fosdick et al., 2015), we assume that the sampled foreland-N deposits are sourced from the Precordillera range, so its elevation was used to determine $P_{hillslope}$ for all foreland-N samples. We assume this is the same for foreland-S samples >2 Ma, but not for the two youngest samples, which contain Frontal Cordillera-derived zircons (see Section 5.4). In this case, we used the Jáchal catchment average elevation (Fig. 2a, 3,410 m). As all wedge-top samples are sourced from the Frontal Cordillera range, we use its 4,000 m average elevation to determine $P_{hillslope}$ for those. Topographic shielding in the study area is <5% (supplementary material), which is within uncertainty of final ^{10}Be production rates and therefore not applied in $P_{hillslope}$.

Lastly, paleo-production rates varied in the past due to secular variations in the strength of the geomagnetic field (Lifton et al., 2014). Currently available calculators of paleo-production rates (i.e. CRONUScalc, Marrero et al., 2016) show up to 50% variability of production rates in the last 2 Ma. Beyond 2 Ma, they are not solvable due to poor resolution of paleo-intensity records (see Balco et al., 2008). Since most of our samples are older than 2 Ma, our calculations do not account for, or include errors associated with, these variations in the geomagnetic field strength because they are unknown. Nonetheless, we point out that variations in paleo-production rates are not capable of generating variability in paleo-erosion rates of the same magnitude as those observed in our data when averaged over >50 ka (supplementary material).

3.1.4 Calculating paleo-erosion rates from ^{10}Be measurements

For studies of modern landscapes, the ^{10}Be concentrations of quartz in alluvium are used to determine the average erosion rate over the quartz-contributing area upstream of the sample point (e.g. Granger et al., 1996). This is possible because the ^{10}Be concentration in active stream sediments is inferred to reflect the residence time of particles in the upper-most meters of Earth's surface (i.e. the erosion rate on the hillslopes; Lal (1991)). We denote this concentration resulting from erosion on the hillslopes as $C_{hillslope}$. Since we measure ^{10}Be concentrations in sandstones in the foreland basin deposits, the measured ^{10}Be concentrations (C_M) contain additional ^{10}Be that was produced during progressive burial of the alluvium (C_{burial}) in the basins (e.g. Clapp et al., 2001), recent exhumation during basin inversion ($C_{exhumation}$), and a period of exposure in outcrop ($C_{exposure}$; see Section 5.1). Thus, the measured ^{10}Be concentration, in at.g^{-1}, is:

$$C_M = \left(C_{hillslope} + C_{burial}\right) \bullet e^{-\lambda t} + C_{exhumation} + C_{exposure} \qquad (1)$$

where t is time (yr) since deposition (i.e. the age of the deposit from magnetostratigraphy), and λ the decay constant for ^{10}Be (5.1 x 10^{-7} a^{-1}; Chmeleff et al., 2010; Korschinek et al., 2010) or ^{26}Al (9.8 x 10^{-7} a^{-1}; Nishiizumi, 2004). Equation 1 is then rewritten in terms of $C_{hillslope}$:

$$C_{hillslope} = \left(C_M - C_{exhumation} - C_{exposure}\right) \bullet e^{\lambda t} - C_{burial} \qquad (2)$$

which yields the concentration due to erosion on the hillslopes at the time of deposition. Once $C_{hillslope}$ is obtained, it can be used to calculate a paleo-erosion rate ($E_{hillslope}$ in cm/a) from:

$$C_{hillslope} = \sum_{i,j,k} \left[\frac{P_{hillslope_{i,j,k}}}{\lambda + (\rho_{hillslope} \bullet E_{hillslope})/\Lambda_{i,j,k}}\right] \qquad (3)$$

where $P_{hillslope(i,j,k)}$ is the average production rate of the source area by each type of ^{10}Be production (spallation (*i*), stopped muons (*j*), fast muons (*k*), in at.g^{-1}.a^{-1}), $\rho_{hillslope}$ the density of the source rocks, assumed to be 2.5 ± 0.3 g.cm^{-3}, $\Lambda_{i,j,k}$ (g.cm^{-2}) are attenuation lengths for each type of production mechanism, adopted as 160 g.cm^{-2} for spallation, 1,500 ± 100 g.cm^{-2} for stopped muons, 5,300 ± 950 g.cm^{-2} for fast muons (Braucher et al., 2003). Equation 3 describes the integral of ^{10}Be production over a particle's path from great depths to the surface. For deep and continuous burial, the equation is similar, thus C_{burial} is:

$$C_{burial} = \sum_{i,j,k} \left[\frac{P_{burial_{i,j,k}}}{\lambda + (\rho_{burial} \bullet A_r)/\Lambda_{i,j,k}}\right] \qquad (4)$$

where $P_{burial(i,j,k)}$ is the production rate at the depositional surface, ρ_{burial} the density of the overburden, assumed to be of uncompacted sand (1.7 ± 0.1 g.cm^{-3}), and A_r the accumulation rate from magnetostratigraphy (cm/a). In this case, A_r is an average from the time of deposition to the time of burial beyond ^{10}Be production by muons.

$C_{exhumation}$ requires sample depth information because we collected samples underneath overburden. Its equation is also similar to equations 3 and 4:

$$C_{exhumation} = \sum_{i,j,k} \left[\frac{P_{outcrop_{i,j,k}} \bullet e^{\frac{-\rho_{ss} \bullet z_{sample}}{\Lambda_{i,j,k}}}}{\lambda + (\rho_{ss} \bullet E_{exhum})/\Lambda_{i,j,k}} \right] \qquad (5)$$

where $P_{outcrop(i,j,k)}$ is the production rate at the outcrop, ρ_{ss} the density of the overlying sandstones (assumed 2.5 ± 0.3 g.cm^{-3}), z_{sample} is the depth of the sample to the top of the outcrop, E_{exhum} the exhumation rate of the basin deposits from thermochronology (cm/a; (Fosdick et al., 2015)). E_{exhum} at foreland-N and the wedge-top was adopted as the mean long-term erosion rates of the Las Salinas anticline (3.1 mm/a, Fig. 4) and of the Frontal Cordillera (1.5 mm/a) respectively (Fosdick et al., 2015). Since there is no thermochronological data from the foreland-S section we calculate the long-term exhumation differently. Here, the deepest stratigraphic units (2,400 m) were exhumed after 1.8 Ma (Milana et al., 2003), which yields a 1.33 mm/a long-term erosion rate at the core of the Mogna anticline (see Fig. 4a). We use the replicate ^{26}Al and ^{10}Be measurements to confirm this estimate (see Section 5.1). At foreland-N and foreland-S, we assume that E_{exhum} is inversely proportional to distance from anticline axis and decrease linearly to zero where rock exposure ends (Table 1).

Lastly, the concentrations accumulated during recent exposure in outcrop can be inferred as:

$$C_{exposure} = t_{outcrop} \bullet S \bullet P_{sample_i} \qquad (6)$$

where $t_{outcrop}$ is the exposure time in the outcrop in years and S is a shielding factor ranging from 0 to 100% depending on outcrop geometry (Gosse and Phillips, 2001). In general, the longer $t_{outcrop}$ is, the higher and less accurate the ^{10}Be paleo-erosion rates become. For this reason, we deem outcrop geometries providing less than 50% shielding as too vulnerable to even short exposure times and discard one of our samples from further interpretation (sample HU-11). Constraints on $t_{outcrop}$ are derived from the ^{26}Al/^{10}Be ratio and a-priori constrains on local exhumation rates.

3.1.5 Error propagation

We performed the calculations described above using a Monte Carlo method for error propagation. We assume that each parameter containing a mean and a standard deviation forms a normal distribution (i.e., P_{source}, P_{burial}, $P_{exhumation}$, λ, sediment density, attenuation lengths, and sample age). We then draw 10,000 random values from each parameter to compute 10,000 possible outcomes of equations 2-6. Finally, a mean $C_{hillslope}$ $\pm 1\sigma$ is obtained from the simulations and used to calculate the paleo-erosion rate. This approach yields uncertainties that are comparable to the standard propagation of errors.

3.2 Detrital zircon U-Pb geochronology

Detrital zircons were extracted from the 60-250 μm grain-size fraction from samples MOG-07 (foreland-S) and HC-07 (foreland-N). Uranium and lead isotopic analysis of zircons was conducted by Laser Ablation Inductively Coupled Plasma Mass Spectrometry. Only analyses with <20% discordance between $^{206}Pb/^{238}U$ and $^{207}Pb/^{235}U$ ages were used for provenance interpretations (n=105 for MOG-07, n=79 for HC-07). Histograms and probability density functions were generated to discretize different crystallization ages (see Section 5.4). Information about analytical methods and data is provided in the supplementary material (Tables A.3-5 and Fig. A.3-6).

4. Assumptions and sensitivity tests

4.1 Paleo-elevations of the sediment source area

By using modern elevations to calculate paleo-production rates we are assuming that the source area did not undergo significant amounts of surface uplift. While there is paleoaltimetry-based evidence that this is true for the wedge-top area (i.e. Hoke et al., 2014), elevations must have changed in the Precordillera after motion of the San Roque and Niquivil thrusts since 8 Ma (Fig. 3a, 4). However, these two thrusts represent ~20% of the areal extent of the Precordillera and largely expose the Cambrian-Ordovician limestones (Fig. 4b). Thus, they cannot have drastically changed the resulting Precordillera hypsometry relevant to cosmogenic nuclides after they uplifted. We demonstrate that this assumption is acceptable by modeling ^{10}Be concentrations for a fixed paleo-erosion rate in an uplifting source-area and inverting the signal back to paleo-erosion rates while assuming constant elevation (Fig. A.7b). This exercise reveals that small temporal changes in mean elevation (i.e. 20%) cause ≤ 30% difference between inferred and true rates (Fig. A.7b). Such difference is well within the range of uncertainty of individual paleo-erosion rates inferred in this study.

4.2 Continuous deposition and exhumation

We assume that the time between sediment entrainment and deposition is unimportant in terms of ^{10}Be production since the distance between the Precordillera and the foreland is typically <40 km. While it is impossible to determine if this assumption is violated, we would expect the pre-depositional exposure time to be different for every sample, which would lead to random temporal patterns of ^{10}Be, which is not what we observe.

We must further assume that burial was quasi-continuous and sediments were not exposed for long periods of time between depositional events given that the temporal resolution of the magnetostratigraphy is > 50 ka. This assumption is acceptable given the high accumulation rates observed in the foreland (Beer, 1990). Similarly, we assume that the recent exhumation phase was also continuous, consistent with sustained high exhumation rates since 3 Ma (Fosdick et al., 2015) and climate change in the Quaternary would only have favored erosion instead of inhibiting it.

Discontinuous deposition cannot be entirely dismissed in the wedge-top deposits. There, the low accumulation rates are the result of hiatuses of uncertain duration either due to erosion or non-deposition (Beer et al., 1990; Ruskin and Jordan, 2007). To minimize these uncertainties, we collected samples at the base of thick sedimentary beds whenever possible and avoided clear evidence of hiatuses in outcrop. After deposition of the sedimentary sequences, the wedge-top valley may have been largely filled by the deposits forming the perched remnant Médano and San Guillermo surfaces (Fig. 2b), which are necessarily younger than 5.2 Ma (youngest unit in wedge-top). This wedge-top fill potentially served as a ≥ 100-meter-thick cap-layer that shielded the deposits in the valley from cosmic rays until their recent excavation. Nonetheless, we show the effects on final paleo-erosion rates for the case where samples were exposed for 100 ka at the base of a 1 m thick layer of sediment prior to being completely buried (supplementary material).

5. Results

5.1 Exposure in outcrop

The foreland-N area has the lowest measured concentrations and is the most sensitive to re-exposure (Table 1). There, the magnetostratigraphic section is broken in two sub-sections that are ~15 km apart (I and II, Fig. 2b). We collected duplicate samples of the same age (7.5 ± 0.1 Ma) along strike: HU-07 (section I) and HU-14 (section II; Table 1). Sample HU-07 was collected in a well-shielded outcrop where cosmic rays are blocked in all directions (S=0) except from muons through the vertical column of rock, which we already corrected for. Its ^{10}Be dose is 1,280 ± 183 at.g^{-1}, while sample HU-14, a much less shielded sample by comparison (S=0.4), has a ^{10}Be dose of 1,734 ± 167 at.g^{-1}. Their concentrations become indistinguishable after correcting for C_{burial}, $C_{exhumation}$, and 135 years of exposure in outcrop ($C_{outcrop}$) using HU-14's shielding geometry and local production rate of ~5.2 at.g^{-1}.a^{-1}. The fact that these samples are ~15 km apart with different shielding geometries and their ^{10}Be budget is matched after minor corrections is strong evidence that these outcrop exposures are short. Lastly, relief within a 120 m radius at all of our sample sites at foreland-N is low and near the noise level of the SRTM 1-arc second data (Fig. A.8). The areas surrounding each outcrop have similar topography and relief, suggesting that outcrop ages must be similar in neighboring areas.

We further constrain exposure times at other locations using the replicate measurements. Overall, the ^{26}Al/^{10}Be ratios in the replicate samples are slightly elevated compared to the expected ratios based solely on C_{burial} and indicate some modern dose (Table 1). This modern dose can be partitioned into exhumation and outcrop exposure components (equations 5 and 6). At foreland-N, 55% of the dose is the result of muogenic production during exhumation of the sections based on the HU-16 replicate (Table 1). This corroborates the rapid exhumation rates inferred from apatite (U-Th-Sm)/He reported by Fosdick et al. (2015). Based on outcrop geometry, the remaining 45% of the modern dose requires 1,000 ± 300 years of exposure, which is higher than the along-strike pair (HU-07 and HU-14), but those are also closer to the Las Salinas anticline. Together, these observations support the assumptions of short exposure time. For foreland-S, our inferred 1.33 mm/a exhumation rate of the Mogna anticline yields a $C_{exhumation}$ higher than that accounted for by the ^{26}Al/^{10}Be measured in MOG-05. Thus, we re-scaled the anticline core exhumation to 2 mm/a, after which $C_{exhumation}$ fully accounts for the modern doses measured in the MOG-05 replicate. This re-scaled exhumation rate is then used as E_{exhum} in the exhumation corrections for the other samples in the Mogna section (Table 1). In the wedge-top, $C_{exhumation}$ accounts for a small portion of the inferred modern dose, thus requiring ~1,700 years of additional exposure in outcrop. The $t_{outcrop}$ inferred above were conservatively applied in all other samples in their respective vicinities (Table 1). A detailed description of the cosmogenic nuclide budget, $t_{outcrop}$ calculation, and further evidence of short outcrop exposure is provided as supplementary material.

5.2 Post-depositional corrections

β ratios $(C_{exhumation}+C_{burial}+C_{exposure})/(C_{hillslope}\bullet e^{-\lambda t})$ are useful for checking what proportion of the measured concentration is made of post-depositional dose; 0.8 has been reported as an acceptable maximum (e.g. Schaller and Ehlers, 2006). β ratios for wedge-top samples are consistently <0.5 for all but the 5.2 Ma sample due to low accumulation rates (Table 1). Four out of nine foreland-N samples yield β ratios ≤ 1 while those at foreland-S are all >1 except for the oldest one (Table 1). In cases where post-depositional doses dominate the measured ^{10}Be concentration, i.e. $\beta > 5$, only a minimum possible paleo-erosion rate was determined from the $C_{hillslope}\bullet e^{-\lambda t} + 1\sigma$ (Table 1). In case all of C_M is removed by post-depositional corrections, minimum rates are calculated from the maximum possible concentration ($1\sigma_M \bullet e^{-\lambda t}$; Table 1). Decay corrections are large and range from a factor of two (2 Ma) to ~46 (7.7 Ma). A supplementary Table A.6 is provided for input in CRONUS online calculator.

5.3 Paleo-erosion rates

Paleo-erosion rates upstream of the wedge-top were ≥ 0.15 mm/a before 7 Ma and decreased below 0.1 mm/a until 5.2 Ma, when they increased back to 0.25 mm/a (+1.2, -0.1; 1σ; Fig. 6a; Table 1). For comparison, we calculated a range of possible paleo-erosion rates using the preserved sediment volumes from seismic imaging of wedge-top deposits (Fig. 6a; Fernández, 1996). We divided the total sediment volumes by the current drainage area of the wedge-top basin (after removing the area of the depocenter) and estimated a total vertical amount of sediment eroded in the catchment for each sequence assuming none of it was recycled from within the basin. This total erosion was then divided by the timespan of each sequence to obtain a long-term paleo-erosion rate (Fig. 6a; Table 2). The range of literature-derived paleo-erosion rates was inferred for hypothetical scenarios in which the deposit volumes were up to 3x greater than those reported by Fernández (1996) (i.e. >100% error on reported values). This conservatively accounts for possible large volumes of erosion during hiatuses. These paleo-erosion rates agree well with the ones obtained using ^{10}Be between 7 and 5.2 Ma.

At foreland-N, the paleo-erosion rates are overall higher than in the wedge-top (Fig. 6b). Here, paleo-erosion rates peak ca. 6.8 Ma at a minimum 1.7 mm/a, which is ~2 Ma after the end of a major pulse of shortening (Fig. 6b). By ca. 4.8 Ma, they decrease to 0.48 mm/a (+0.19, -0.1; 1σ), increase again to 0.75 (+0.44, - 0.2; 1σ) and drop dramatically to 0.03 ± 0.01 mm/a ca. 3.2 Ma (Fig. 6b). It is interesting to note that the foreland-N paleo-erosion rates increase when rates in the wedge-top decrease coeval with higher wedge-top accumulation rates (i.e. 7-5.2 Ma; Fig. 6a, b). Meanwhile, paleo-erosion rates at foreland-S ranged from ~0.06 mm/a (+0.02, -0.01; 1σ) ca. 7.5 Ma to ~1.14 mm/a (+2.57, -0.47;

1σ) ca. 4.8 Ma, higher than foreland-N at that time (Fig. 6c). Rates then reached 2.4 mm/a (+5.7, -1; 1σ) ca. 2 Ma and remained high or potentially increased ca. 1.8 Ma, however, a meaningful paleo-erosion rate cannot be recovered due to a very low ^{10}Be dose (Table 1; Fig. 6c).

Table 1. ^{10}Be and ^{26}Al data and paleo-erosion rates

A_r - accumulation rates; E_m - E_{exhum} (modern strat. section erosion rate); C_M - measured concentration; C_b - C_{burial} (^{10}Be); C_{exh} - $C_{exhumation}$ (^{10}Be); C_{hill} - $C_{hillslope}$ (^{10}Be); z - depth below top of outcrop; S - scaling coefficient; β - $(C_{ex}+C_{expo}+C_b)/C_{hill}\bullet e^{-\lambda t}$; t_{oc} – $t_{outcrop}$; E - paleo-erosion rate. Concentrations are for ^{10}Be unless otherwise indicated.

Sample	Age[a] (Ma)	A_r (mm/a)	E_m[b] (mm/a)	C_M x10^3 (at.g^{-1}) ^{10}Be		C_M x10^3 (at.g^{-1}) ^{26}Al		$^{26}Al/^{10}Be$		$C_b\bullet e^{-\lambda t}$ x10^3 (at.g^{-1})		C_{exh} x10^3 (at.g^{-1})		C_{expo} x10^3 (at.g^{-1})		C_{hill} x10^3 (at.g^{-1})		z cm	S	β	t_{oc} yr	E mm/a		
foreland-N				μ	1σ	μ	1σ	μ	1σ	μ	1σ	μ	1σ	μ	1σ	μ	1σ					μ	+1σ	-1σ
HU-11[c,d]	8.8	0.88	2.9	4.06	0.2	-	-	-	-	-	-	-	-	-	-	-	-	100	0.7	-	-	-	-	-
HU-13	7.8	0.94	2.6	1.88	0.15	-	-	-	-	0.17	0.04	0.50	0.14	-	-	65.16	19.3	600	0	0.50	-	0.24	0.10	0.05
HU-07	7.5	0.92	2.7	1.73	0.17	-	-	-	-	0.19	0.04	0.49	0.14	-	-	28.98	13.9	600	0	1.12	-	0.53	0.49	0.17
HU-14	7.5	0.89	2.5	1.28	0.18	-	-	-	-	0.21	0.05	0.65	0.16	0.28	0.02	27.78	13.8	250	0.4	1.90	135	0.56	0.55	0.18
HU-15	6.9	0.74	2.5	1.25	0.17	-	-	-	-	0.34	0.07	0.66	0.17	0.11	0.01	5.12	9.21	250	0.2	8.10	135	1.4[e]	-	-
HU-02	6.2	0.32	2.3	2.64	0.35	-	-	-	-	1.11	0.22	0.64	0.17	-	-	22.27	13.3	410	0	1.94	-	0.69	1.04	0.26
HU-16	4.8	0.47	2.3	5.52	0.53	11.4	2.66	2.1	0.5	1.55	0.26	0.60	0.16	0.53	0.05	32.06	8.91	500	0.1	0.70	1000	0.48	0.19	0.10
HU-05	4	0.46	2.0	8.39	0.64	-	-	-	-	2.38	0.37	0.77	0.20	2.63	0.23	20.54	7.60	330	0.5	2.20	1000	0.75	0.44	0.20
HU-17	3.2	0.35	1.7	95.6	3.3	-	-	-	-	4.68	0.66	0.80	0.22	2.63	0.23	445.27	49.0	500	0.5	0.09	1000	0.03	0.01	0.01
foreland-S																								
MOG-02	7.5	0.51	1.2	6.34	0.34	-	-	-	-	0.35	0.08	0.56	0.23	2.35	0.20	248.3	58.4	2000	0.4	0.16	-	0.06	0.02	0.01
MOG-05[c]	4.9	0.28	0.8	5.99	0.41	14.6	3.53	2.5	0.6	3.24	0.56	1.67	0.44	-	-	13.61	9.41	489	0.3	1.18	-	1.14	2.57	0.47
MOG-09	1.9	0.21	0.4	22.3	2.17	-	-	-	-	14.7	1.86	2.88	0.74	2.94	0.25	12.56	8.80	350	0.5	3.75	-	2.44	5.72	1.01
MOG-07	1.7	0.21	0.4	16.9	0.82	-	-	-	-	16.2	2.04	3.16	0.85	-	-	-	1.95	500	0.5	-	-	-	-	-
wedge-top																								
ANG-04	7.6	0.15	1.5	13.1	0.55	-	-	-	-	2.02	0.47	1.27	0.33	7.79	0.66	104.12	64.5	400	0.5	5.55	1700	0.38	0.62	0.15
R1-02	7.1	0.22	1.5	13.5	0.68	-	-	-	-	1.71	0.38	1.29	0.34	3.89	0.33	259.96	71.9	360	0.5	1.04	1700	0.15	0.06	0.03
MD-02[f]	6.8	0.28	1.5	36.9	1.44	-	-	-	-	1.64	0.42	0.02	0.03	-	-	1170.7	296.6	1000	0	0.04	1700	0.03	0.01	0.01
R1-01	6.8	0.22	1.5	25.6	1.05	66.3	7.9	2.6	0.3	2.05	0.43	1.27	0.33	7.44	0.64	472.09	105.2	400	0.5	0.47	1700	0.08	0.02	0.02
ANG-07	6.3	0.3	1.5	28.7	1.32	-	-	-	-	1.91	0.38	1.26	0.33	7.79	0.67	457.90	96.1	400	0.5	0.61	1700	0.09	0.02	0.02
ANG-02	5.2	0.03	1.5	59.6	2.2	-	-	-	-	40.4	7.59	1.23	0.32	7.79	0.66	160.34	132.3	450	0.5	4.88	1700	0.25	1.18	0.11

a. Magnetostratigraphic age (Johnson et al., 1986; Jordan et al., 2001, 1993; Milana et al., 2003; Ruskin and Jordan, 2007). Each age was propagated through with a 0.1 Ma error.

b. Long-term erosion rates obtained from Fosdick et al. (2015).

c. Grain size fraction: 100-500 μm

d. Sample is poorly shielded and not used for interpretation.

e. Minimum possible rate based on $C_{hillslope}$+1σ.

f. This sample is located at the base of the fill forming the Médano paleosurface (Fig. 2b). Age was obtained through U-Pb analysis on zircons from a tuffaceous sandstone sample collected directly below. See Table A.5 for results from U-Pb analysis.

Table 2: Preserved sequence volumes in the wedge-top reported by Fernández (1996) and inferred erosion rates (this study)

Stratigraphic sequence	Age[a] (Ma)	Timespan (Ma)	Compacted vol. (km^3)	Vol./Area[b] (km)	Erosion rate (mm/a or km/Ma)		
	8.69				1x Vol.	2x Vol.	3x Vol.
3	7.65	1.04	109.62	0.02	0.01	0.02	0.03
4	6.93	0.72	187.31	0.04	0.03	0.05	0.08
5	6.56	0.37	163.06	0.03	0.04	0.09	0.13
6	5.2	1.4	123.9	0.02	0.01	0.02	0.03

a. Age of top of sequence

b. Wedge-top catchment area is 10,000 km^2

5.4 Detrital zircons

The two detrital zircon samples for U-Pb crystallization ages help evaluate changes in source areas. At 1.8 Ma in foreland-S, detrital zircon ages are prominently centered ca. 231-258 Ma (Fig. 7a). At 7.1 Ma in foreland-N, detrital zircon ages yield a pronounced age population of 290-320 Ma (Fig. 7b). Both samples yield less prominent early Paleozoic and Proterozoic zircons. Following the interpretation of sources by Fosdick et al. (2015), we attribute the pronounced 290-320 Ma age-peaks present in the 7.1 Ma sandstone to recycling of Lower Permian strata eroded from the Precordillera. Furthermore, we attribute the considerably younger 231-258 Ma age-peaks to erosion of the Permo-Triassic Choiyoi Group that dominates the Frontal Cordillera, upstream of the wedge-top (Fig. 4a).

6. Discussion

6.1 Evidence in favor of a tectonic control of mass fluxes

The first distinction between climate and tectonic drivers we can make is based on the erosional signature of foreland-N (Fig. 6b). If climate changes were governing mass fluxes, we would expect high erosion rates in the wedge-top followed by a retreat of the deformation front (i.e. narrowing of the wedge). The opposite behavior is observed in the Precordillera (Fig. 3a, 6), where deformation continues to propagate into the Bermejo basin today (Fosdick et al., 2015). Higher river discharge related to climate change could theoretically lead to increased erosion everywhere (Braun et al., 2015). There is little evidence of long-lasting climatic shifts in and around the study area (Latorre et al., 1997; Ruskin and Jordan, 2007; Hynek et al., 2012; Cotton et al., 2014; Hoke et al., 2014) that could sustain the high erosion rates from 7.5 to 4 Ma observed in foreland-N (Fig. 3d, 6b). More importantly, erosion rates would vary similarly in all of the studied sections if that were the case. Nonetheless, increased seasonality in the Pliocene (Latorre et al., 1997) may have contributed to changes in erosion rates; however the periodicity and magnitude of such changes (Godard et al., 2013) would be irresolvable in our data due to the temporal resolution of the magnetostratigraphy and uncertainties in determining paleo-erosion rates this old (Schaller and Ehlers, 2006). Lastly, most of the evidence of early glaciers in Argentina is from the Late Miocene - Early Pliocene and hundreds of kilometers south of the study area (Fig. 3e; Mercer, 1983). In the latitudes of the study area, glaciers are localized, inefficient erosion agents (Bissig et al., 2002), and thus an unlikely cause for our observed low ^{10}Be concentrations, especially at foreland-S ca. 2 Ma. For these reasons, we discard the hypothesis that erosion rates are primarily controlled by shifts in climate.

6.2 Evidence in favor of a tectonic control of base-level

The observed factor of five difference in erosion rates between foreland-N and the wedge-top until 5.2 Ma indicates that sediment sources were independent and that erosion was focused in the actively deforming Precordillera. These findings are consistent with the shift in provenance records showing dominance of Precordillera-derived recycled Carboniferous zircons and sharp decrease in Frontal Cordillera-derived Choiyoi zircons starting ca. 10 Ma and lasting at least until ca. 7.1 Ma during and after the major pulse of crustal shortening (Fig. 6, 7; Fosdick et al., 2015).

Since erosion was focused in the uplifted hanging walls of the Precordillera thrusts, we suggest that thrust activity caused fluvial disconnection between the wedge-top and the foredeep as proposed by Beer et al. (1990) (Fig. 8). If this is the case, then the wedge-top must have been internally-drained, suggesting that the perched paleo-surfaces now being consumed by knickpoints are geomorphic remnants of a former wedge-top fill (Fig. 8b). This interpretation is consistent with a tectonic control of local base-level in which thrust-motion favors the formation and filling of internally drained wedge-top basins as proposed for another intermontane basin to the NE (Hilley and Strecker, 2005). Although our data is not sufficient to confirm hydrologic isolation, it still indicates that the wedge-top's base-level fluctuated. For example, during periods of low accumulation rates (or hiatuses), the paleo-erosion rates inferred in this study are higher than those derived using Fernández's (1996) reported sequence volumes (Fig. 6a). This suggests that the formation of hiatuses could be coeval with higher erosion in the wedge-top rather than non-deposition and, thus, could be caused by base-level fall. It is unknown, however, if the wedge-top remained isolated or if it overflowed into the neighboring intermontane valley to the south. The available $\delta^{18}O$ and $\delta^{13}C$ in local lake deposits within the wedge-top do not allow to test for hydrologic isolation (Ruskin and Jordan, 2007). Nonetheless, the presence of evaporitic deposits alone suggests some degree of basin isolation (Fig. 5c; Ruskin and Jordan, 2007).

If the wedge-top became fluvially isolated from the foreland during deformation in the Precordillera, at some point it reconnected to form the modern landscape (Fig. 8c). We suggest that this reconnection is evident in our data based on the migration of rapid erosion from the Precordillera to the Frontal Cordillera (in the upstream direction) between 5.2 and 2 Ma. The reported change in sedimentary facies ca. 4 Ma at foreland-S (Milana et al., 2003) to a permanent axial river is consistent with the sharp decline in paleo-erosion rates observed ca. 3.2 Ma at foreland-N followed by an increase ca. 2 Ma at foreland-S. Combined with the reappearance of abundant Choiyoi detrital zircons from the Frontal Cordillera ca. 2 Ma, the coeval change in sedimentary facies and trade-off between paleo-erosion rates in the two foreland sections suggests the southward deflection of the Río Jáchal and the reestablishment of its fluvial connectivity with the wedge-top (Fig. 8b, c). Here, we stress that most of the older foreland basin strata contain low proportions of Choiyoi zircons. Thus, old foreland strata are only secondary sources for the substantial resurgence of this age population in 1.8 Ma deposits at foreland-S (Levina et al., 2014; Fosdick et al., 2015).

If the observations outlined above do imply reconnection with the wedge-top after 5 Ma, then the post-2 Ma ^{10}Be signal at foreland-S must be an admixture of recycled wedge-top sediments and sediments sourced from the actively eroding Precordillera and Frontal Cordillera. Given the age range of the wedge-top strata, at least two half-lives of ^{10}Be decay occurred prior to being remobilized and deposited at foreland-S. Combined with the higher long-term erosion rates from the Precordillera and Frontal Cordillera (Fosdick et al., 2015), the low ^{10}Be concentration at foreland-S is plausible.

6.3 Lagged erosional response to tectonic shortening

In the stream power construct, upstream migration of higher erosion rates coincides with the propagation of knickpoints through a catchment. Whether generated by rock uplift or base-level fall, knickpoints migrate upstream as a wave that separates the fast and slowly eroding parts of the landscape (Whipple and Tucker, 1999). Since ^{10}Be concentrations in alluvium average over the entire upstream area, the mean ^{10}Be concentration reflects the proportion of sediments derived from those fast and slowly eroding parts of the landscape. After the erosional wave covers half the catchment, ^{10}Be erosion rates reach a maximum, lagging behind its trigger mechanism (Willenbring et al., 2013). We observe a > 2 Ma lag between erosion and shortening maxima at foreland-N (Fig. 6b). Combined with the later shift in provenance to a Frontal Cordillera source, this leads us to the interpret our data to reflect the time necessary for an erosion wave, which initiated at the thrust-front (i.e. knickzone), to migrate through the Precordillera and remove most of the ^{10}Be-rich, relict upper meter of rock (Willenbring et al., 2013). In this case, the occurrence of resistant limestones at the toes of the distal thrusts (Fig. 4), as well as continued thrusting, likely slowed these knickzones down and contributed to the observed lag.

Ultimately, it is the erosional efficiency, particularly modulated by precipitation, that rules an orogen's response time after an external perturbation (Stolar et al., 2006; Whipple and Meade, 2006). Perhaps it is not surprising that the Precordillera took at least 2 Ma to reach its peak catchment-wide erosion rate under a semi-arid climate. Despite a long response time, the observed high erosion rates sustained from 7.5 to 4 Ma (Fig. 6b) are consistent with an erosional response to structural widening of critical tapers. This suggests that modeling efforts, such as those by Stolar et al. (2006) and Whipple and Meade (2006), accurately capture the overall nature of this system. However, the existence of a time-lag as predicted by Willenbring et al. (2013) and observed here may represent a way in which the transients (i.e. erosion and rock-uplift) are decoupled, thus deviating from Whipple and Meade's (2006) and Stolar et al.'s (2006) predictions (Fig. 1b). This in turn suggests that the assumption of self-similar growth at constant taper angles may not always be appropriate, at least for arid orogens.

7. Conclusion

We extracted cosmogenic ^{10}Be paleo-erosion rates from exhumed Upper Miocene-Pliocene foreland basin strata. The range of paleo-erosion rates observed in this study is typical of catchment-wide erosion rates in tectonically active areas both globally and locally (Pepin et al., 2013; Portenga and Bierman, 2011; Walcek and Hoke, 2012). The paleo-erosion rates reveal an ~2 Ma lagged catchment-wide maximum in erosion relative to the end of a major period of tectonic forcing as predicted by Willenbring et al. (2013). Moreover, this lag is followed by sustained, high rates of erosion as envisaged by

Whipple and Meade (2006) and Stolar et al. (2006). Based on the magnitude of the observed lag, we conclude that semi-arid transient landscapes, such as the Precordillera, preserve geomorphic signals of base-level perturbation over Ma timescales. This implies that average catchment ^{10}Be measurements may reflect perturbations that occurred millions of years earlier. Lastly, given the temporal and spatial dynamics of erosion observed in this study, we conclude that, in areas of similarly dry climate, structural widening of orogenic wedges is followed by erosional lags and sustained high erosion rates. During this period, headward waves of erosion may outpace wedge-widening and migrate from the active thrust-front, across the wedge-top basin, and ultimately into the core of the orogen.

Acknowledgements

We thank: 1) the donors of the American Chemical Society Petroleum Research Fund for support of this research (award 52480-DNI8 to G. Hoke); 2) CAPES/Science Without Borders (Brazilian Government) for a Doctoral Fellowship to P. Val (Project #0515-12-4); 3) U.S. National Science Foundation for funds to support U-Pb geochronology (Award EAR-1049605 to J. Fosdick); 4) T. Jordan and B. Ruskin for providing detailed stratigraphic section locations; 5) H. Canelo and G. Ortiz for field support; 6) C. Schulz and J. Bartel for laboratory support at GFZ; 7) B. Wilkinson and D. McPhillips for insightful discussions. We are grateful to P. Bierman, B. Fisher, D. Granger and three anonymous reviewers for constructive comments on the manuscript as it evolved.

Appendix A. Supplementary material

Supplementary data to this article can be found online.

FIGURE CAPTIONS

Fig. 1. Contrasting models of erosional response to external perturbations in an orogenic wedge (a-b) and in a catchment (c). W&M’ 06 denotes Whipple and Meade (2006) and W’13 denotes Willenbring et al. (2013). The gray rectangles mark the period of perturbation in each model. Colored lines denote the erosional response and black lines denote rock uplift rates. Magnitudes of changes in erosion and uplift rates were not kept to scale; only temporal variations matter. Note that the perturbation in c corresponds to a wave of uplift entering the catchment in the headwaters and exiting at its outlet. (For interpretation of the references to color in this figure legend, the reader is referred to the web version of this article.)

Fig. 2. (a) Location of the study area showing tectonic provinces (colored polygons), outline of the Jáchal catchment (black line), outline of the assumed Precordillera paleo-catchment, and depths to subducting Nazca plate (solid white lines; Cahill and Isacks, 1992). The black rectangle shows the location of Fig. 2b; (b) Topographic map from a 90 m digital elevation model (http://srtm.csi.cgiar.org). Note that the foreland-N section is composed of two sub-sections. The wedge-top sub-basins are indicated by R (Rodeo) and Ang (Angualasto). The Médano (M) and San Guillermo (SG) paleosurfaces are outlined (solid white line). (c) Hypsometry of the Jáchal catchment and of the two major tectonic provinces as outlined in Fig. 2a. Note that hypsometry of the Frontal Cordillera contains a large area of intermontane, wedge-top valleys. (For interpretation of the references to color in this figure legend, the reader is referred to the web version of this article.)

Fig. 3: Summary of tectonic (a, b), sedimentary (c), climatic (d), and other important events in South America (SA; e), such as the timing of flat-slab subduction and glaciation and inferred formation of the perched paleo-surfaces outlined in Fig. 2b. Abbreviations in (a) are: FC – Frontal Cordillera; CN – Cerro Negro; Tr – Tranca thrust; C – Caracol

thrust; B – Blanco thrust; Bq – Blanquitos thrust; SR – San Roque thrust; N – Niquivil thrust; NA – Niquivil anticline; SA – Las Salinas anticline. Thrusts are outlined in Fig. 4a, except FC (not mapped at the surface).

Fig. 4. (a) Simplified bedrock geology based on published maps (Cardó and Díaz, 1999; Furque et al., 1998). Labeled, solid black lines are traces of major thrust faults. Sampled stratigraphic sections are marked by dashed red lines. (b) Modified structural cross-section of the area based on literature (line shown in Fig. 4a; Allmendinger and Judge, 2014; Cardó and Díaz, 1999; Fosdick et al., 2015; Zapata and Allmendinger, 1996). (For interpretation of the references to color in this figure legend, the reader is referred to the web version of this article.)

Fig. 5. Stratigraphic positions for each sample. a) foreland-N (Johnson et al., 1986; Jordan et al., 2001, 1993); b) foreland-S (Milana et al., 2003); c) simplified wedge-top (Ruskin and Jordan, 2007). Samples R1-01 and R1-02 belong to the Rodeo sub-basin in the wedge-top (section not shown; see open circles for accumulation; locations shown in Fig. 2b) and are positioned in the profile based on age. Sample MD-02, also positioned by age, was collected from the base of the Médano surface (Fig. 2b, 3). Note difference in scales for section thicknesses. (For interpretation of the references to color in this figure legend, the reader is referred to the web version of this article.)

Fig. 6. Observed patterns of sediment accumulation and shortening history from literature (Allmendinger and Judge, 2014; Jordan et al., 2001; Milana et al., 2003; Ré et al., 2003; Ruskin and Jordan, 2007), and inferred paleo-erosion rates determined in this study (squares) with 1σ uncertainty envelopes. (a) wedge-top paleo-erosion rates show opposite pattern to the foreland-N curve (b). Green band shows range of possible erosion rates using the volumes of deposits in the wedge-top (see Section 5.3 for details; Fernández, 1996); (b) foreland-N results. Locus of erosion: Precordillera (see text). (c) foreland-S results show a pronounced increase in erosion rates ca. 2 Ma. Locus of erosion: wedge-top, Precordillera, and Frontal Cordillera (see Section 5.4). Numbers in parenthesis

denote 1σ uncertainty where they fall out of the plot. (For interpretation of the references to color in this figure legend, the reader is referred to the web version of this article.)

Fig. 7. Probability density plot of detrital zircons (black line) from this study at foreland-S (Mogna Fm.) ca. 1.8 Ma (a) and at foreland-N (Río Jáchal Fm.) ca. 7.1 Ma (b) showing the relative contributions of each grain age. Colored bands highlight the age range for different sources (color-coded as in Fig. 4). 0-3.5 Ga plots are provided in Fig. A.3-6. Data from Fosdick et al. (2015) are shown for comparison (c-e).

Fig. 8. Conceptual model for landscape evolution of the study area as interpreted in this study overlain on the present day's topography. Blue arrows show hypothesized main fluvial flow directions. The San Roque and Niquivil thrusts are the only structures outlined but other Precordillera thrusts were active during the periods highlighted (Fig. 3a). Faint contours are in 1 km (black) and 0.5 km (gray) intervals. Wedge-top fill depicted in (b) was obtained by interpolation of low-slope alluvial surfaces in the wedge-top. Paleo-surfaces: Médano (M) and San Guillermo (SG). (For interpretation of the references to color in this figure legend, the reader is referred to the web version of this article.)

References

Allmendinger, R.W., Figueroa, D., Snyder, D., Beer, J., Mpodozis, C., Isacks, L., 1990. Foreland shortening and crustal balancing in the Andes at 30° S Latitude. Tectonics 9, 789–809. http://dx.doi.org/10.1029/TC009i004p00789

Allmendinger, R.W., Judge, P.A., 2014. The Argentine Precordillera: A foreland thrust belt proximal to the subducted plate. Geosphere 10, 1203–1218. doi:10.1130/GES01062.1

Balco, G., Stone, J.O., Lifton, N.A., Dunai, T.J., 2008. A complete and easily accessible means of calculating surface exposure ages or erosion rates from ^{10}Be and ^{26}Al

measurements. Quat. Geochronol. 3, 174–195. doi:http://dx.doi.org/10.1016/j.quageo.2007.12.001

Beer, J.A., 1990. Steady Sedimentation and Lithologic Completeness, Bermejo Basin, Argentina. J. Geol. 98, 501–517. http://www.jstor.org/stable/30065610

Beer, J.A., Allmendinger, R.W., Figueroa, D.E., Jordan, T.E., 1990. Seismic stratigraphy of a Neogene piggyback basin, Argentina. Am. Assoc. Pet. Geol. Bull. 74, 1183–1202.

Bissig, T., Clark, A.H., Lee, J.K.W., Hodgson, C.J., 2002. Miocene Landscape Evolution and Geomorphologic Controls on Epithermal Processes in the El Indio-Pascua Au-Ag-Cu Belt, Chile and Argentina. Econ. Geol. 97, 971–996. http://dx.doi.org/10.2113/gsecongeo.97.5.971

Braucher, R., Brown, E.T., Bourlès, D.L., Colin, F., 2003. In situ produced ^{10}Be measurements at great depths: Implications for production rates by fast muons. Earth Planet. Sci. Lett. 211, 251–258. doi:10.1016/S0012-821X(03)00205-X

Braun, J., Voisin, C., Gourlan, a T., Chauvel, C., 2015. Erosional response of an actively uplifting mountain belt to cyclic rainfall variations. Earth Surf. Dyn. 1–14. doi:10.5194/esurf-3-1-2015

Cahill, T., Isacks, B.L., 1992. Seismicity and Shape of the Subducted Nazca Plate. J. Geophys. Res. Solid Earth 97, 17503–17529. http://dx.doi.org/10.1029/92JB00493

Cardó, R., Díaz, I.N., 1999. Hoja Geológica 3169-I, Rodeo. Boletín 272. SEGEMAR Inst. Geol. y Recur. Miner., Buenos Aires.

Charreau, J., Blard, P.-H., Puchol, N., Avouac, J.-P., Lallier-Vergès, E., Bourlès, D., Braucher, R., Gallaud, a., Finkel, R., Jolivet, M., Chen, Y., Roy, P., 2011. Paleo-erosion rates in Central Asia since 9Ma: A transient increase at the onset of Quaternary glaciations? Earth Planet. Sci. Lett. 304, 85–92. doi:10.1016/j.epsl.2011.01.018

Chmeleff, J., von Blanckenburg, F., Kossert, K., Jakob, D., 2010. Determination of the ^{10}Be half-life by multicollector ICP-MS and liquid scintillation counting. Nucl. Instruments Methods Phys. Res. Sect. B Beam Interact. with Mater. Atoms 268, 192–199. doi:10.1016/j.nimb.2009.09.012

Clapp, E.M., Bierman, P.R., Nichols, K.K., Pavich, M., Caffee, M., 2001. Rates of sediment supply to arroyos from upland erosion determined using in situ produced cosmogenic ^{10}Be and ^{26}Al. Quat. Res. 55, 235–245. doi:10.1006/qres.2000.2211

Cotton, J.M., Hyland, E.G., Sheldon, N.D., 2014. Multi-proxy evidence for tectonic control on the expansion of C4 grasses in northwest Argentina. Earth Planet. Sci. Lett. 395, 41–50. doi:10.1016/j.epsl.2014.03.014

Dahlen, F.A., 1990. Critical taper model of fold-and-thrust belts and accretionary wedges. Annu. Rev. Earth Planet. Sci. 18, 55–99. http://dx.doi.org/10.1146/annurev.ea.18.050190.000415

Fernández, A., 1996, Seismic analysis, paleoclimatology, and fluvial architecture of the Bermejo Basin, central Andes, western Argentina [Ph.D. Dissertation], Cornell University; Ithaca, New York, U.S.A. 279 p.

Fosdick, J.C., Carrapa, B., Ortíz, G., 2015. Faulting and erosion in the Argentine Precordillera during changes in subduction regime: Reconciling bedrock cooling and detrital records. Earth Planet. Sci. Lett. 432, 73–83. doi:10.1016/j.epsl.2015.09.041

Furque, G., González, P., Caballé, M., 1998. Hoja Geológica 3169-II, San José de Jáchal

(Províncias de San Juan y La Rioja). Escala 1:250,000. SEGEMAR Inst. Geol. y Recur. Miner., vol 259, pp 1-83

Garver, J.I., Brandon, M.T., Roden-Tice, M., Kamp, P.J.J., 1999. Exhumation history of orogenic highlands determined by detrital fission-track thermochronology, in: Ring, U., Brandon, M.T., Lister, G.S., Willet, S.D. (Eds.), Exhumation Processes: Normal Faulting, Ductile Flow and Erosion. Geological Society Special Publications, London UK, pp. 283–304.

Gehrels, G., 2011. Detrital Zircon U-Pb Geochronology: Current Methods and New Opportunities, in: Tectonics of Sedimentary Basins. John Wiley & Sons, Ltd, pp. 45–62. doi:10.1002/9781444347166.ch2

Godard, V., Tucker, G.E., Burch Fisher, G., Burbank, D.W., Bookhagen, B., 2013. Frequency-dependent landscape response to climatic forcing. Geophys. Res. Lett. 40, 859–863. doi:10.1002/grl.50253

Goethals, M. M., R. Hetzel, S. Niedermann, H. Wittmann, C. R. Fenton, P. W. Kubik, M. Christl, and F. von Blanckenburg (2009), An improved experimental determination of cosmogenic ^{10}Be/^{21}Ne and ^{26}Al/^{21}Ne production ratios in quartz, *Earth Planet. Sci. Lett.*, *284*(1–2), 187–198, doi:10.1016/j.epsl.2009.04.027.

Gosse, J.C., Phillips, F.M., 2001. Terrestrial in situ cosmogenic nuclides: theory and application. Quat. Sci. Rev. 20, 1475–1560. doi:10.1016/S0277-3791(00)00171-2

Granger, D.E., Kirchner, J.W., Finkel, R., 1996. Spatially averaged long-term erosion rates measured from in situ-produced cosmogenic nuclides in alluvial sediment. J. Geol. 104, 249–257. http://www.jstor.org/stable/30068190

Hilgen, F.J., Lourens, L.J., Dam, J.A. Van, Beu, A.G., Boyes, A.F., Cooper, R.A., Krijgsman, W., Ogg, J.G., Piller, W.E., Wilson, D.S., 2012. Chapter 29 - The Neogene Period, in: Gradstein, F.M., Schmitz, J.G.O.D., Ogg, G.M. (Eds.), The Geologic Time Scale. Elsevier, Boston, pp. 923–978. doi:http://dx.doi.org/10.1016/B978-0-444-59425-9.00029-9

Hilley, G.E., Strecker, M.R., 2005. Processes of oscillatory basin filling and excavation in a tectonically active orogen: Quebrada del Toro Basin, NW Argentina. Geol. Soc. Am. Bull. 117, 887. doi:10.1130/B25602.1

Hoke, G.D., Giambiagi, L.B., Garzione, C.N., Mahoney, J.B., Strecker, M.R., 2014. Neogene paleoelevation of intermontane basins in a narrow, compressional mountain range, southern Central Andes of Argentina. Earth Planet. Sci. Lett. 406, 153–164. doi:10.1016/j.epsl.2014.08.032

Hynek, S. a., Passey, B.H., Prado, J.L., Brown, F.H., Cerling, T.E., Quade, J., 2012. Small mammal carbon isotope ecology across the Miocene-Pliocene boundary, northwestern Argentina. Earth Planet. Sci. Lett. 321–322, 177–188. doi:10.1016/j.epsl.2011.12.038

Johnson, N.M., Jordan, T.E., Johnsson, P.A., Naeser, C.W., 1986. Magnetic polarity stratigraphy, age and tectonic setting of fluvial sediments in an eastern Andean foreland basin, San Juan Province, Argentina. Spec. Publs int. Ass. Sediment. 8, 63–75. http://dx.doi.org/10.1002/9781444303810.ch3

Jordan, T.E., Allmendinger, R.W., Damanti, J.F., Drake, R.E., 1993. Chronology of Motion in a Complete Thrust Belt: The Precordillera, 30-31° S, Andes Mountains. J. Geol. 101, 135–156. http://www.jstor.org/stable/30081144

Jordan, T.E., Schlunegger, F., Cardozo, N., 2001. Unsteady and spatially variable evolution of the Neogene Andean Bermejo foreland basin, Argentina. J. South Am. Earth Sci. 14, 775–798. doi:10.1016/S0895-9811(01)00072-4

Kooi, H., Beaumont, C., 1996. Large-scale geomorphology: Classical concepts reconciled and integrated with contemporary ideas via a surface processes model. J. Geophys. Res. 101, 3361. doi:10.1029/95JB01861

Korschinek, G., Bergmaier, A., Faestermann, T., Gerstmann, U.C., Knie, K., Rugel, G., Wallner, A., Dillmann, I., Dollinger, G., von Gostomski, C.L., Kossert, K., Maiti, M., Poutivtsev, M., Remmert, A., 2010. A new value for the half-life of ^{10}Be by Heavy-Ion Elastic Recoil Detection and liquid scintillation counting. Nucl. Instruments Methods Phys. Res. Sect. B Beam Interact. with Mater. Atoms 268, 187–191. doi:10.1016/j.nimb.2009.09.020

Lal, D., 1991. Cosmic ray labeling of erosion surfaces: in situ nuclide production rates and erosion models. Earth Planet. Sci. Lett. 424–439. http://dx.doi.org/10.1016/0012-821X(91)90220-C

Latorre, C., Quade, J., McIntosh, W.C., 1997. The expansion of C4 grasses and global change in the late Miocene: Stable isotope evidence from the Americas. Earth Planet. Sci. Lett. 146, 83–96. doi:10.1016/S0012-821X(96)00231-2

Levina, M., Horton, B.K., Fuentes, F., Stockli, D.F., 2014. Cenozoic sedimentation and exhumation of the foreland basin system preserved in the Precordillera thrust belt (31–32°S), southern central Andes, Argentina. Tectonics 33, 1659–1680. doi:10.1002/2013TC003424

Lifton, N., Sato, T., Dunai, T.J., 2014. Scaling in situ cosmogenic nuclide production rates using analytical approximations to atmospheric cosmic-ray fluxes. Earth

Planet. Sci. Lett. 386, 149–160. doi:10.1016/j.epsl.2013.10.052

Marrero, S., Phillips, F., Borchers, B., Lifton, N., 2016. Cosmogenic Nuclide Systematics and the CRONUScalc Program. Quat. Geochronol. 31, 1–72. doi:10.1016/j.quageo.2015.09.005

Mercer, J.H., 1983. Cenozoic Glaciation in The Southern Hemisphere. Ann. Rev. Earth Planet Sci. 11, 99–132. http://dx.doi.org/10.1146/annurev.ea.11.050183.000531

Milana, J.P., Bercowski, F., Jordan, T., 2003. Paleoambientes y magnetoestratigrafía del Neógeno de la Sierra de Mogna , y su relación con la Cuenca de Antepaís Andina. Rev. la Asoc. Geológica Argentina 58, 447–473.

Nishiizumi, K., 2004. Preparation of ^{26}Al AMS standards. Nucl. Instruments Methods Phys. Res. Sect. B Beam Interact. with Mater. Atoms 223–224, 388–392. doi:10.1016/j.nimb.2004.04.075

Nishiizumi, K., Imamura, M., Caffee, M.W., Southon, J.R., Finkel, R.C., McAninch, J., 2007. Absolute calibration of ^{10}Be AMS standards. Nucl. Instruments Methods Phys. Res. Sect. B Beam Interact. with Mater. Atoms 258, 403–413. doi:10.1016/j.nimb.2007.01.297

Pepin, E., Carretier, S., Hérail, G., Regard, V., Charrier, R., Farías, M., García, V., Giambiagi, L., 2013. Pleistocene landscape entrenchment: A geomorphological mountain to foreland field case, the Las Tunas system, Argentina. Basin Res. 25, 613–637. doi:10.1111/bre.12019

Phillips, F.M., Argento, D.C., Balco, G., Caffee, M.W., Clem, J., Dunai, T.J., Finkel, R., Goehring, B., Gosse, J.C., Hudson, A.M., Jull, A.J.T., Kelly, M.A., Kurz, M., Lal, D., Lifton, N., Marrero, S.M., Nishiizumi, K., Reedy, R.C., Schaefer, J., Stone, J.O.H., Swanson, T., Zreda, M.G., 2015. The CRONUS-Earth Project: A Synthesis. Quat. Geochronol. doi:10.1016/j.quageo.2015.09.006

Portenga, E.W., Bierman, P.R., 2011. Understanding Earth's eroding surface with ^{10}Be. GSA Today 21, 4–10. doi:10.1130/G111A.1

Rahl, J.M., Ehlers, T. a., van der Pluijm, B. a., 2007. Quantifying transient erosion of orogens with detrital thermochronology from syntectonic basin deposits. Earth Planet. Sci. Lett. 256, 147–161. doi:10.1016/j.epsl.2007.01.020

Ramos, V. A., E. O. Cristallini, and D. J. Perez (2002), The Pampean flat-slab of the Central Andes, J. South Am. Earth Sci., 15 (1), 59–78. doi:10.1016/S0895-9811(02)00006-8.

Ré, G.H., Jordan, T.E., Kelley, S., 2003. Cronología y paleogeografía del Terciario de la Cuenca Intermontana de Iglesia septentrional, Andes de San Juan, Argentina. Rev. la Asoc. Geológica Argentina 58, 31–48.

Ruskin, B.G., Jordan, T.E., 2007. Climate Change Across Continental Sequence Boundaries: Paleopedology and Lithofacies of Iglesia Basin, Northwestern Argentina. J. Sediment. Res. 77, 661–679. doi:10.2110/jsr.2007.069

Schaller, M., Ehlers, T. a., 2006. Limits to quantifying climate driven changes in denudation rates with cosmogenic radionuclides. Earth Planet. Sci. Lett. 248, 153–167. doi:10.1016/j.epsl.2006.05.027

Siame, L.L., Bourlès, D.L., Sébrier, M., Bellier, O., Carlos Castano, J., Araujo, M., Perez, M., Raisbeck, G.M., Yiou, F., 1997. Cosmogenic dating ranging from 20 to 700 ka of a series of alluvial fan surfaces affected by the El Tigre fault, Argentina. Geol. 25, 975–978. doi:10.1130/0091-7613(1997)025<0975:CDRFTK>2.3.CO;2

Stolar, D.B., Willett, S.D., Roe, G.H., 2006. Climatic and tectonic forcing of a critical orogen. Tectonics, Clim. Landsc. Evol. 398, 241–250. doi:10.1130/2006.2398(14).

von Blanckenburg, F., Belshaw, N.S., O'Nions, R.K., 1996. Separation of ^{9}Be and cosmogenic ^{10}Be from environmental materials and SIMS isotope dilution analysis. Chem. Geol. 129, 93–99. doi:10.1016/0009-2541(95)00157-3

Walcek, A.A., Hoke, G.D., 2012. Surface uplift and erosion of the southernmost Argentine Precordillera. Geomorphology 153–154, 156–168. doi:10.1016/j.geomorph.2012.02.021

Whipple, K., Meade, B., 2006. Orogen response to changes in climatic and tectonic forcing. Earth Planet. Sci. Lett. 243, 218–228. doi:10.1016/j.epsl.2005.12.022

Whipple, K.X., 2009. The influence of climate on the tectonic evolution of mountain belts. Nat. Geosci. 2, 97–104. doi:10.1038/ngeo413

Whipple, K.X., Tucker, G.E., 1999. Dynamics of the stream-power river incision model: Implications for height limits of mountain ranges, landscape response timescales, and research needs. J. Geophys. Res. 104, 17661–17674. http://dx.doi.org/10.1029/1999JB900120

Whittaker, A.C., Boulton, S.J., 2012. Tectonic and climatic controls on knickpoint retreat rates and landscape response times. J. Geophys. Res. Earth Surf. 117. http://dx.doi.org/10.1029/2011JF002157

Willenbring, J.K., Gasparini, N.M., Crosby, B.T., Brocard, G., 2013. What does a mean mean? The temporal evolution of detrital cosmogenic denudation rates in a transient landscape. Geology 41, 1215–1218. doi:10.1130/G34746.1

Zapata, T.R., Allmendinger, R.W., 1996. Growth stratal records of instantaneous and progressive limb rotation in the Precordillera thrust belt and Bermejo basin, Argentina. Tectonics 15, 1065–1083. doi:10.1029/96TC00431

FIGURES

Figure 1 (single column)

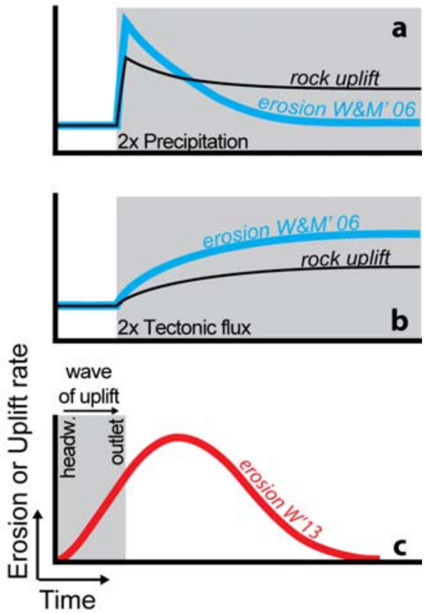

Figure 2 (double column)

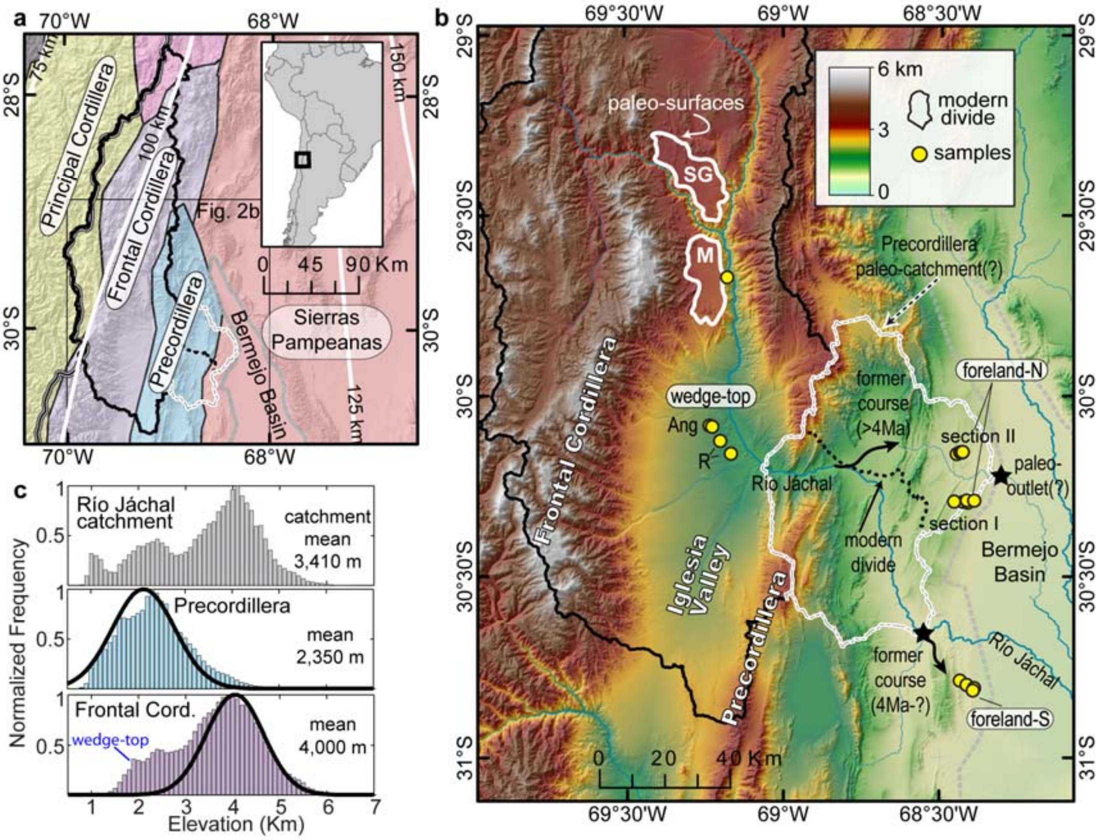

906

907

Figure 3 (1.5 column)

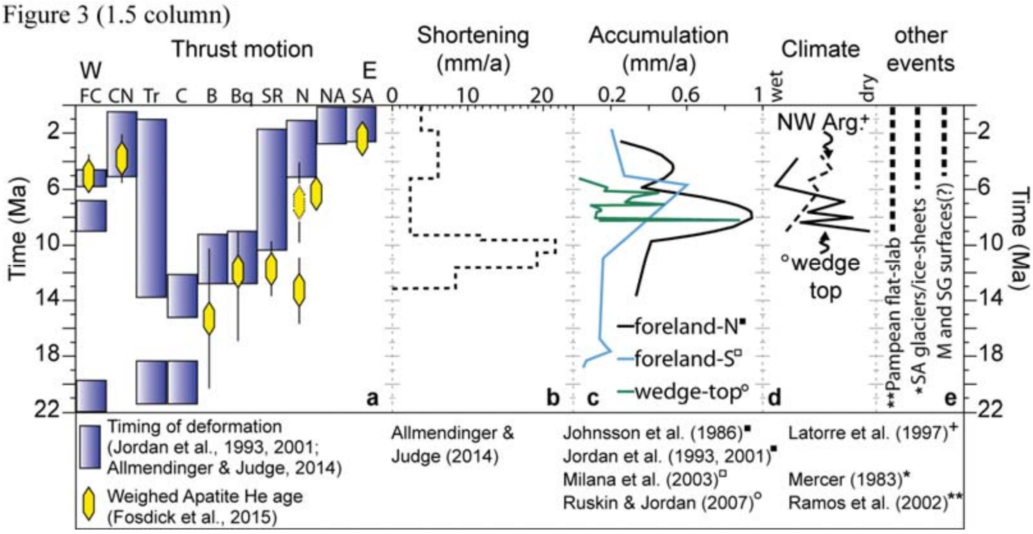

Figure 4 (1.5 column)

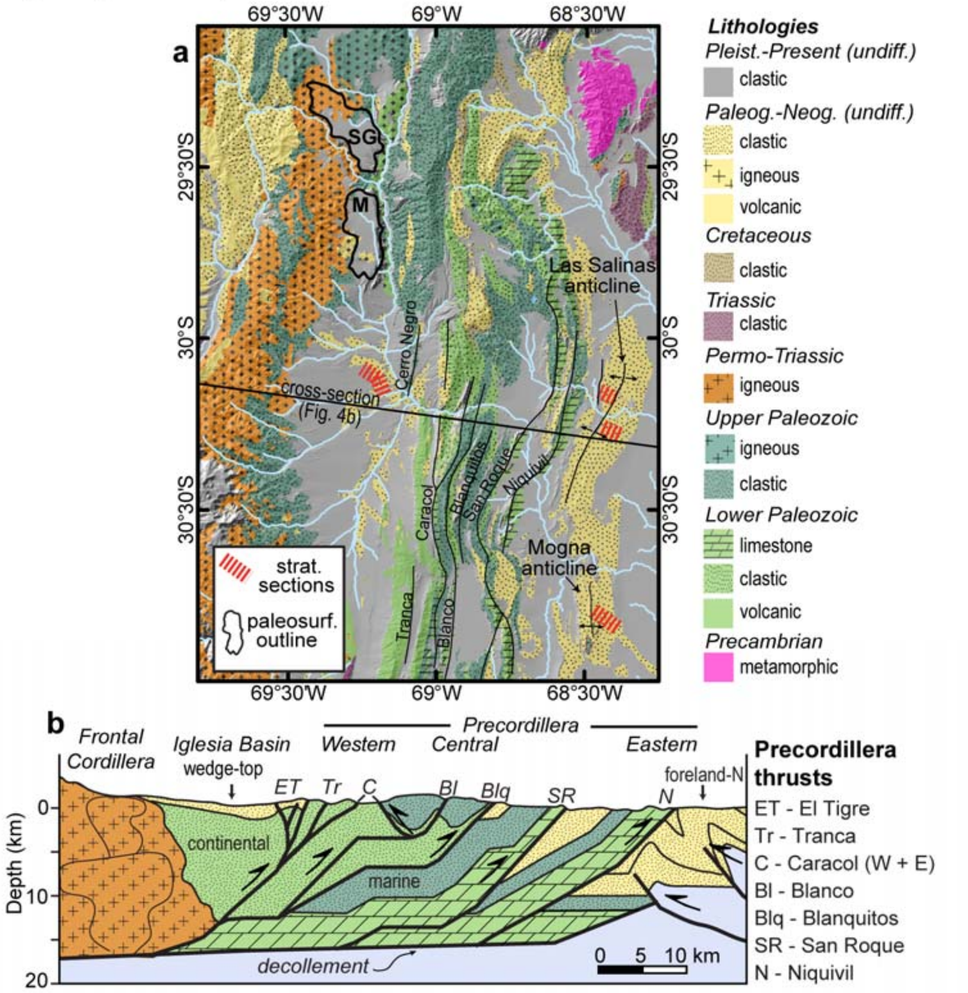

Figure 5 (double column)

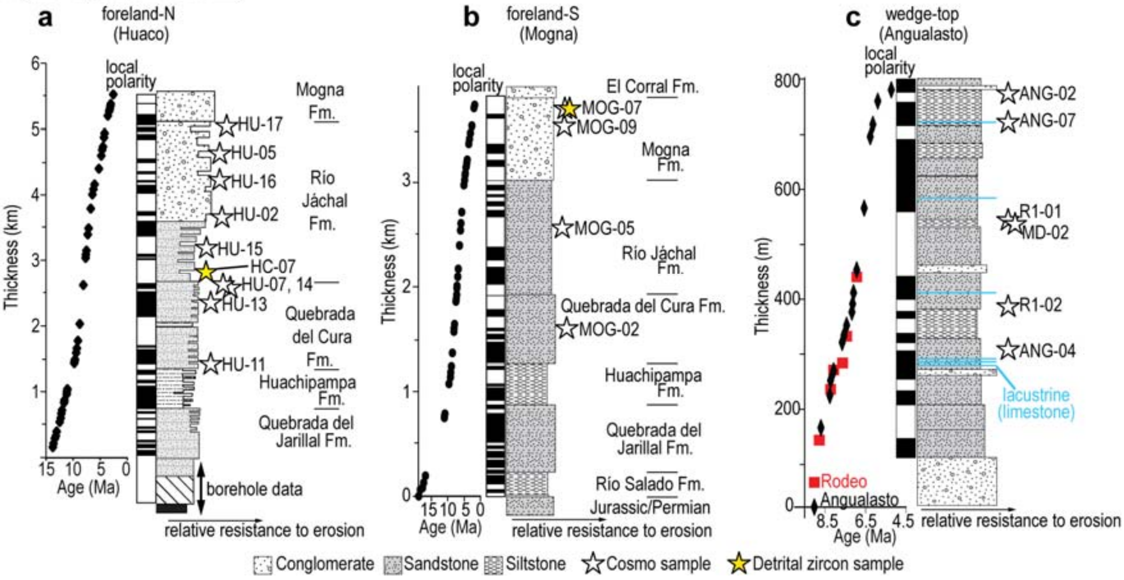

Figure 6 (single column)

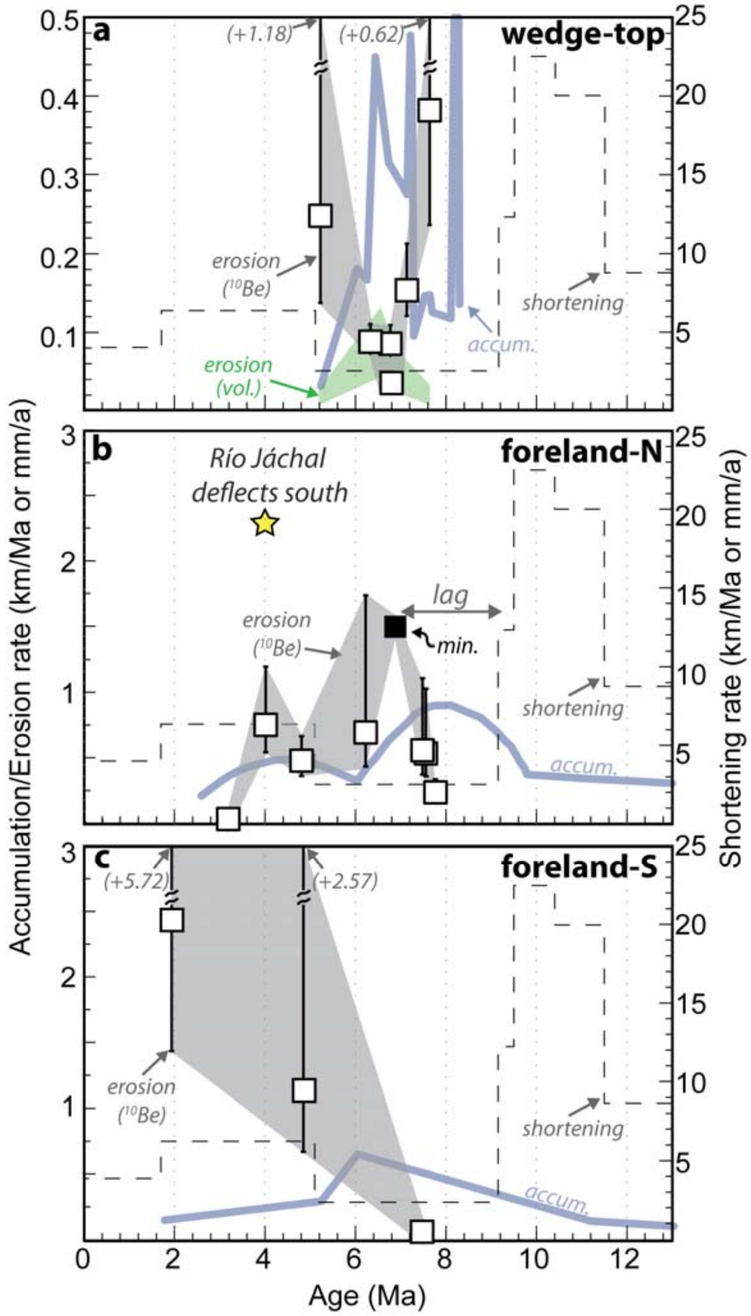

914

915

Figure 7 (single column)

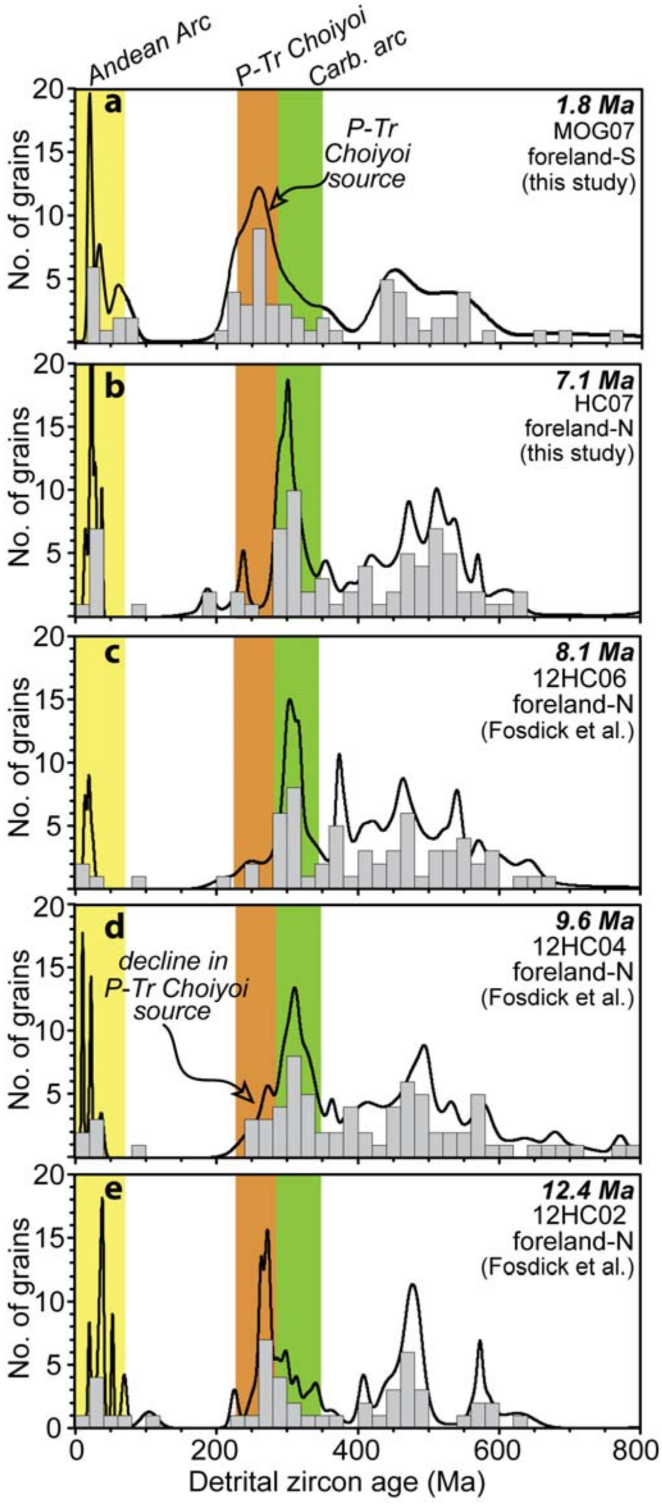

Figure 8 (double column)

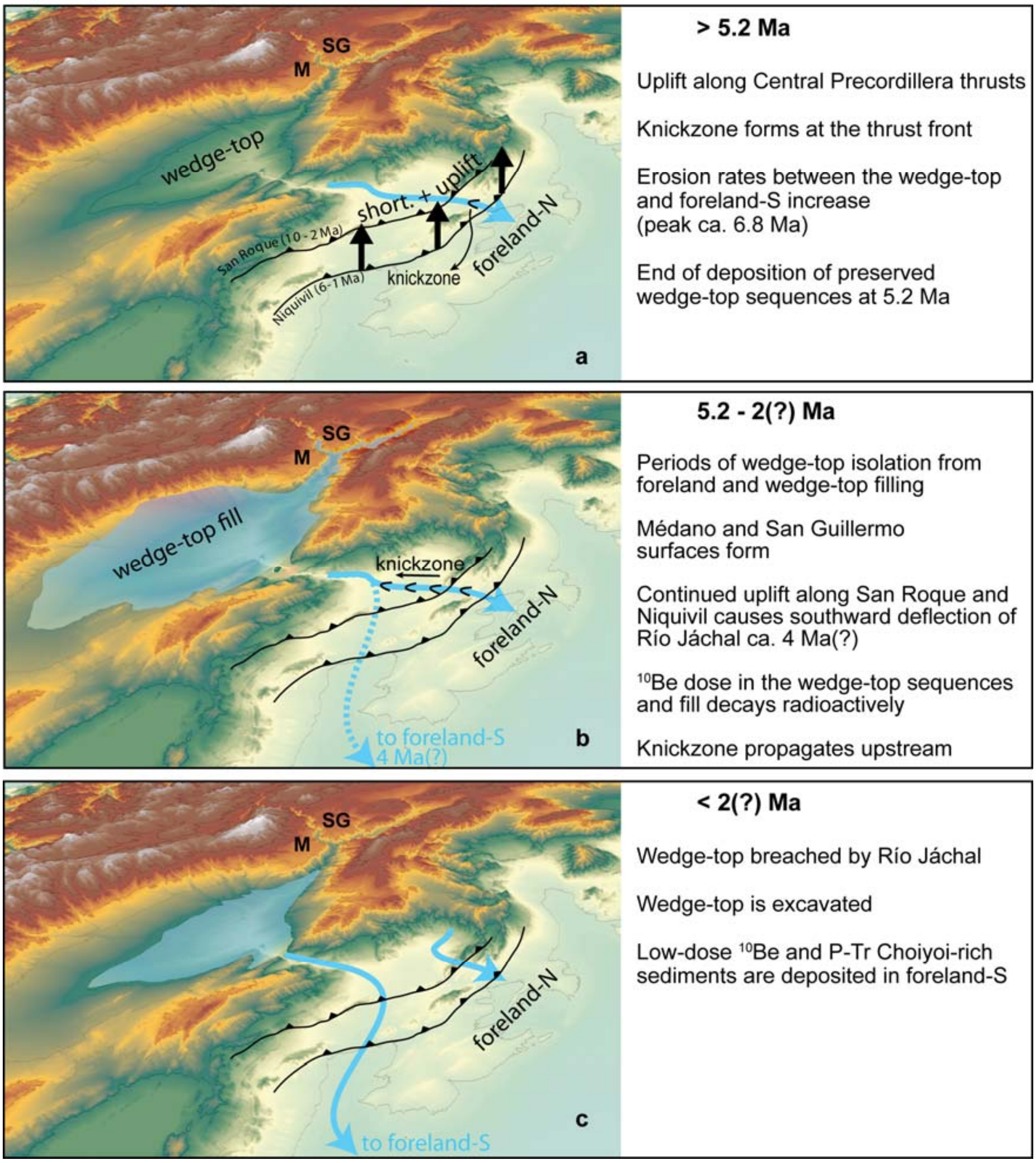

Reconciling tectonic shortening, sedimentation and spatial patterns of erosion from ^{10}Be paleo-erosion rates in the Argentine Precordillera

Pedro Val, Gregory D. Hoke, Julie C. Fosdick, Hella Wittmann

Supplementary Material

Detrital zircon U-Pb geochronology

Detrital zircons were extracted from ~5 kg medium-grained sandstone hand-samples using standard mineral separation techniques, including crushing and grinding, fractionation of magnetic minerals with a Frantz isodynamic magnetic separator, and settling through heavy liquids to exclude phases with densities less than 3.3 g/cm^3. Final zircon separates were mounted in epoxy resin and polished to expose interiors of grains. 127 grains from MOG-07 were selected at random for U-Pb isotopic analysis through Laser-Ablation Multicollector Inductively Coupled Plasma Mass Spectrometry (LA-ICPMS) at Boise State University relative to standards Plešovice zircon (Sláma et al., 2008). For sample HC-07, 110 grains were selected randomly for U-Pb isotopic analysis through LA-ICPMS at the University of Arizona relative to the Sri Lanka zircon standard following standard methods (Gehrels et al., 2006). Calculated U-Pb ages use the $^{206}Pb/^{238}U$ ratio for >900 Ma grains and the $^{206}Pb/^{207}Pb$ ratio for <1.0 Ga grains. Detrital zircon U-Pb analytical data for samples MOG-07 and HC-07 are summarized in Table A.3 and A.4, respectively.

At BSU, zircons were analyzed using a ThermoElectron X-Series II quadrupole ICPMS and New Wave Research UP0213 Nd:YAG UV (213 nm) laser ablation system (Rivera et al., 2013). For U-Th-Pb age analysis, instrumental fractionation of the background-subtracted $^{206}Pb/^{238}U$, $^{207}Pb/^{206}Pb$, and $^{208}Pb/^{232}Th$ ratios is corrected, and ages calibrated with respect to interspersed measurements of the Plešovice zircon standard (Sláma et al., 2008). Signals at mass 204 are indistinguishable from zero following subtraction of mercury backgrounds measured during the gas blank (< 1000 cps ^{202}Hg), thus ages are reported without common Pb correction; however, age error propagation includes an uncertainty contribution due to common Pb using the absolute value of the measured $^{206}Pb/^{204}Pb$ ratio. Secondary standards measured as unknown yielded ages within error of accepted values (Arizona Sri Lanka—563.5 Ma; R33—419.2 Ma; Zirconia—327.2 Ma; Fish Canyon Tuff—28.4 Ma).

At the University of Arizona, U-Pb detrital zircon geochronology was conducted through LA–ICPMS following the methods of Gehrels et al. (2006). Detrital zircons were randomly analyzed from a linear swath of grains across the sample mount to minimize sampling bias in characterizing all detrital populations. Zircons were ablated using a New Wave DUV193 Excimer laser (operating at a wavelength of 193 nm) using a spot diameter of 50 μm. Each analysis lasted for 20 s, during which a pit ~20 μm in depth is excavated. U and Pb isotopes from the ablated material was measured simultaneously using a Micromass Isoprobe in static mode, using Faraday detectors for ^{238}U, ^{232}Th, and ^{208}Pb–^{206}Pb and an ion-counting channel for ^{204}Pb. Common Pb corrections are made by using the measured ^{204}Pb and assuming initial Pb composition from (Stacey and Kramers, 1975). In-run analysis of zircon grains of known isotopic and U-Pb composition (every fifth to sixth measurement) is used to correct for this fractionation. Concordia diagrams and relative-age-probability diagrams were constructed using the software of Ludwig (2008) (figures A.4, A.6).

Effects of ignoring time-dependent production rates on inferred paleo-erosion rates

Using CRONUScalc (Marrero et al., 2016), we compute a temporal signal of ^{10}Be for two different paleo-erosion rate histories (0.2 mm/a and 0.3 mm/a) and a constant burial at 0.5 mm/a using time-dependent production rates. We then infer those paleo-erosion rates while assuming a constant production rate to assess the effects of potential variations in production rates past 2 Ma (Fig. A.7a). The results show that, averaged over >50 ka, time-dependent production rates can generate variable structure in the paleo-erosion rates if assumed time-independent, but these variations are generally ≤ 20%, which is smaller than the uncertainties of the paleo-erosion rates inferred in this study (Table 1).

Effects of assuming constant catchment elevation on inferred paleo-erosion rates

We generated a ^{10}Be signal for a source area eroding at 0.2 mm/a and uplifting from 1800 m ca. 8 Ma to 2350 m ca. 3 Ma using Equation 3 in the main text. We also used an arbitrary burial rate of 0.5 mm/a at ~800 m, which is similar the accumulation rates observed in foreland-N. The signals are then inverted back to paleo-erosion rates through the same steps described in Section 3.1.4 in the main text while assuming the modern elevation (2350 m) remained unchanged through time. Two important predictions arise if this assumption is violated: 1) paleo-erosion rates deviate from the true (input) paleo-erosion rate in a systematic manner similar to the variation in source-area elevation; 2) for a 20% change in mean elevation, inferred paleo-erosion rates only marginally deviate from true (input) paleo-erosion rates (Fig. A.7b).

Further evidence of short outcrop exposure times in the wedge-top

The crucial assumption that our samples have only been marginally affected by recent exposure of the stratigraphic sections combined with ^{10}Be concentrations on the order of 10^3 at.g^{-1} warrants discussion. While we are able to constrain what outcrop exposure may look like based on ^{26}Al and ^{10}Be data from one replicate sample from each section, we provide further evidence in support of minimal recent exposure.

Similar to the foreland area, we expect recent exposure to be short in the wedge-top due to ongoing excavation of the valley. For example, there is ~1 km of fluvial incision now separating the perched Médano and San Guillermo paleo-surfaces (Fig. 2b in main text). Moreover, parts of the stratigraphic sections were uplifted and exposed along blind-thrusts of the El Tigre fault system, which was active ca. ≤ 300 ka (Siame et al., 1997), making them particularly vulnerable to erosion. Lastly, outcrops in the wedge-top usually contain rock-fall, indicating that they are unstable. Taken together with the ~1,700 years of outcrop exposure, these reasons point to low recent exposure in the wedge-top.

Using ^{26}Al/^{10}Be to infer $t_{outcrop}$ and E_{exhum}

In this section, we describe how we use the replicate samples to infer $t_{outcrop}$. Of the three replicate samples, the youngest is 4.8 Ma and the oldest, 7.7 Ma. Thus, we expect low ^{26}Al/^{10}Be ratios for all three. Sample HU-16 (4.8 Ma) is well shielded in outcrop and yielded a ratio of 2.1 ± 0.5 (1σ), which is higher than the expected ratio of 0.8 ± 0.2 (1σ) we infer for a sample of this age that was gradually buried at 0.47 mm/a. This observation indicates that this sample contains ~1,100 at.g^{-1} and ~7,430 at.g^{-1} of modern ^{10}Be and ^{26}Al, respectively. The production of modern ^{10}Be due to exhumation accounts for ~600 at.g^{-1}. Since this sample is 90% shielded in outcrop and the outcrop production rate is 5.2 at.g^{-1}.yr^{-1}, it takes ~1,000 years to produce 500 at.g^{-1}. We use this exposure time as a possible maximum age for nearby outcrops in the foreland-N section and conservatively apply this correction to samples HU-05, HU-16, and HU-17.

Sample MOG-05 (4.8 Ma) is relatively well shielded in outcrop and yielded a ^{26}Al/^{10}Be ratio of 2.5 ± 0.6 (1σ), which is also higher than the expected ratio of 0.8 ± 0.2 (1σ). The excess ^{10}Be and ^{26}Al concentrations responsible for this deviation is 1,600 at.g^{-1} and 11,070 at.g^{-1}, respectively. The inferred $C_{exhumation}$ for the 1.33 mm/a exhumation rate assumed for the Mogna anticline was 2,550 ± 690 at.g^{-1}, which is higher than the inferred modern. Thus, to reach 1,600 at.g^{-1} the local exhumation rate (E_{exhum}) must be 0.8 mm/a, not 0.5 mm/a. Based on our assumption of the geometry of exhumation for the anticline cores, the exhumation rate at the core of the Mogna anticline must be 2 mm/a, not 1.33 mm/a as inferred initially. The re-scaled exhumation rates for all samples were used to calculate $C_{exhumation}$ in this section and are shown in Table 1 in the main text. We do not attempt to determine $t_{outcrop}$ here since it would imply even higher exhumation rates and at this point our inferences would be somewhat arbitrary. Thus, $C_{exposure}$ is not calculated for the Mogna section.

Sample R1-01 (6.7 Ma) yielded a $^{26}Al/^{10}Be$ ratio of 2.59 ± 0.33 (1σ), which is much higher than an expected ratio of 0.34 ± 0.12 (1σ). This implies some modern exposure of the sample, which was collected from an outcrop wall with 50% shielding. To lower the $^{26}Al/^{10}Be$ from ~2.6 to 0.34, one needs to subtract ~9,000 at.g^{-1} of ^{10}Be and ~60,750 at.g^{-1} of ^{26}Al from the measured concentrations after the burial correction, assuming a modern ratio of 6.75. The ^{10}Be in $C_{exhumation}$ accounts for ~1,400 ± 445 at.g^{-1} of ^{10}Be, which leaves ~7,750 at/g^{-1} unaccounted for. With 50% outcrop shielding and an outcrop production rate of 8.75 at.g^{-1}.yr^{-1}, this excess dose requires ~1,770 years of exposure in outcrop. We also take this exposure time as a maximum for the wedge-top area and incorporate the correction when calculating $C_{exposure}$ for all wedge-top samples.

References

Gehrels, G., Valencia, V., Pullen, A., 2006. Detrital zircon geochronology by laser-ablation multicollector ICPMS at the Arizona LaserChron Center. Paleontol. Soc. Pap. 12, 67.

Granger, D.E., Muzikar, P.F., 2001. Dating sediment burial with in situ-produced cosmogenic nuclides: theory, techniques, and limitations. Earth Planet. Sci. Lett. 188, 269–281. doi:10.1016/S0012-821X(01)00309-0

Ludwig, K.R., 2008. Isoplot/Ex 3.6: A geochronological toolkit for Microsoft Excel. Berkeley Geochronologic Cent. Spec. Publ. 4, 77.

Marrero, S., Phillips, F., Borchers, B., Lifton, N., 2016. Cosmogenic Nuclide Systematics and the CRONUScalc Program. Quat. Geochronol. 31, 1–72. doi:10.1016/j.quageo.2015.09.005

Rivera, T. a., Storey, M., Schmitz, M.D., Crowley, J.L., 2013. Age intercalibration of $^{40}Ar/^{39}Ar$ sanidine and chemically distinct U/Pb zircon populations from the Alder Creek Rhyolite Quaternary geochronology standard. Chem. Geol. 345, 87–98. doi:10.1016/j.chemgeo.2013.02.021

Sláma, J., Košler, J., Condon, D.J., Crowley, J.L., Gerdes, A., Hanchar, J.M., Horstwood, M.S. a, Morris, G. a., Nasdala, L., Norberg, N., Schaltegger, U., Schoene, B., Tubrett, M.N., Whitehouse, M.J., 2008. Plešovice zircon - A new natural reference material for U-Pb and Hf isotopic microanalysis. Chem. Geol. 249, 1–35. doi:10.1016/j.chemgeo.2007.11.005

Stacey, J.S., Kramers, J.D., 1975. Approximation of terrestrial lead isotope evolution by a two-stage model. Earth Planet. Sci. Lett. 26, 207–221. doi:10.1016/0012-821X(75)90088-6

FIGURES

A.1 Photographs of sampled outcrops showing outcrop geometry.

A.2 Outline of low-quartz lithologies

A.3 0-2.5 Ga results for MOG-07

A.4 Concordia diagram from sample MOG-07

A.5 0-2.5 Ga results for HC-07

A.6 Concordia diagram from sample HC-07

A.7 Testing the sensitivity of the assumption constant production and elevation through time.

A.8 Relief of the foreland-N area.

A.9 Paleo-erosion rate results for hypothetical hiatus in the wedge-top.

A.10: Histogram of scaling factors obtained pixel by pixel using a 90 m resolution SRTM DEM. Note that the majority of scaling factors is higher than 98%.

TABLES

A.1 ^{10}Be AMS results

A.2 ^{26}Al AMS and ICP-OES results

A.3 Detrital zircon U-Pb analytical data and geochronology, sample MOG-07

A.4 Detrital zircon U-Pb analytical data and geochronology, sample HC-07

A.5 Detrital zircon U-Pb analytical data and geochronology, sample MD-01

A.6 Table for input in CRONUS online calculator. ^{10}Be concentrations are the estimated concentrations relative to paleo-erosion rates ($C_{hillslope}$).

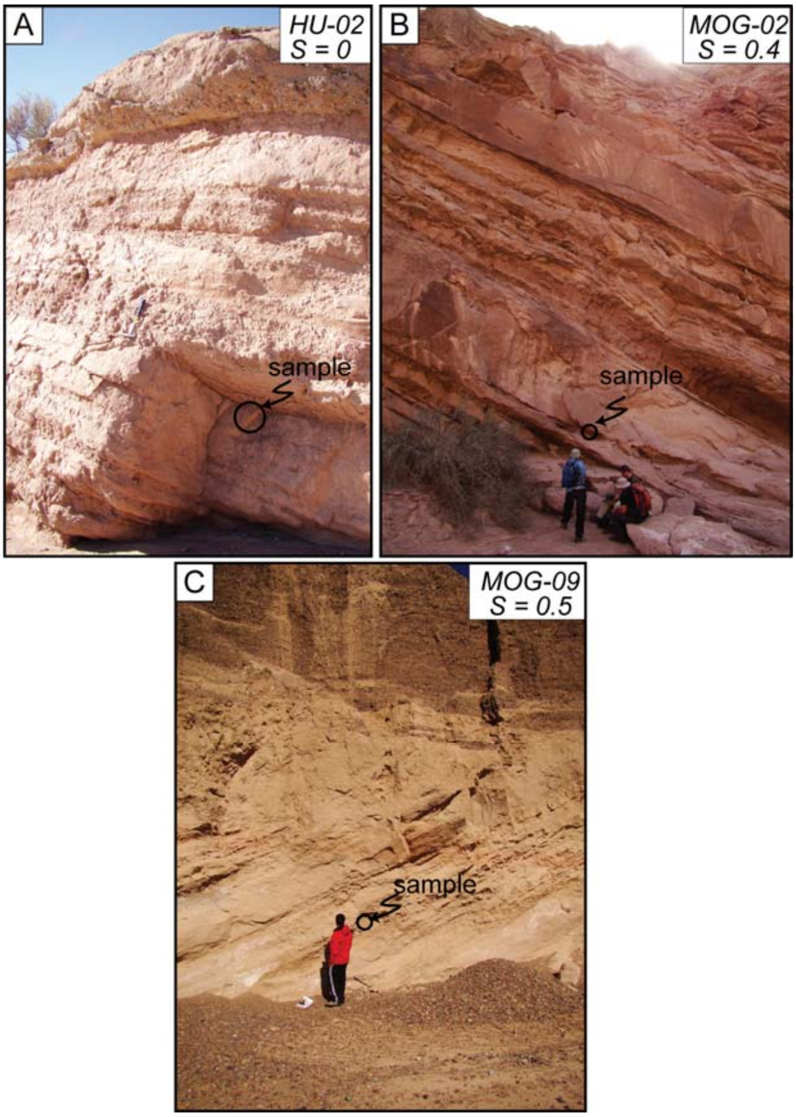

Fig. A.1 Photographs of sampled outcrops showing shielding geometries. Sample names and adopted *S* values for equation S2 is shown in the upper right corner. A) Ideal case in which the sample is completely shielded by the outcrop geometry (see hammer for scale). B) Example in a 30 m deep canyon. The vertical wall provides half the shielding, and the surrounding topography constitutes about an overall 40° angle to the horizon, providing another 10% of shielding. C) Example of an exposed wall without shielding by surrounding topography.

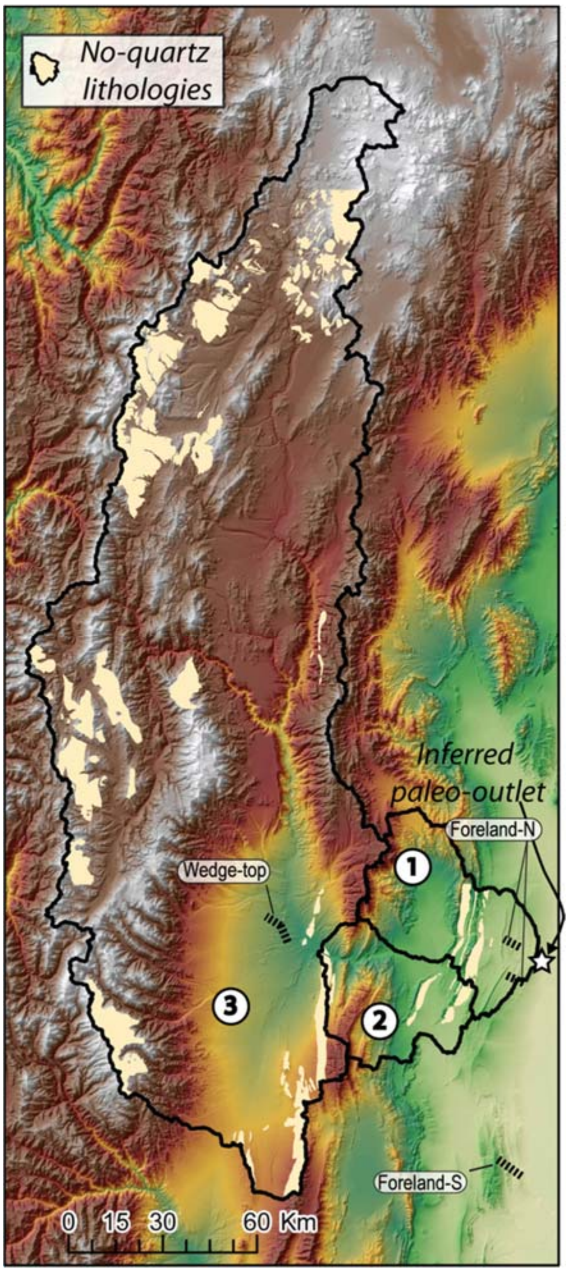

Fig. A.2 Idealized Río Jáchal catchment with outlet near Huaco. Catchment #3 was used in production rate calculations for wedge-top samples. Catchment #2 is the downstream extension of catchment #3, i.e. the Río Jáchal catchment. Catchment #1 is the Huaco catchment. The entire area outlined in black yields the catchment wide scaling factors and production rates depicted in figure S2.

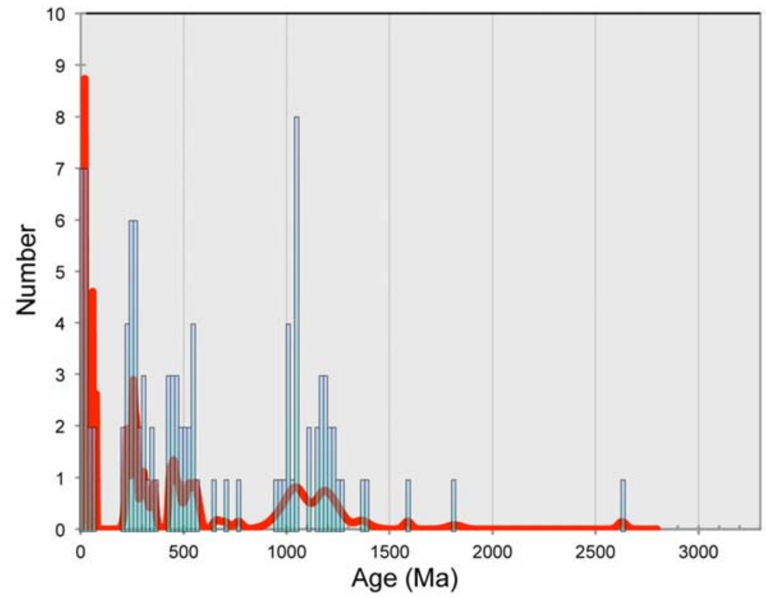

Fig. A.3 0-2.5 Ga results for MOG-07 (1.8 Ma) detrital zircon sample from the Mogna Fm., Foreland-S section.

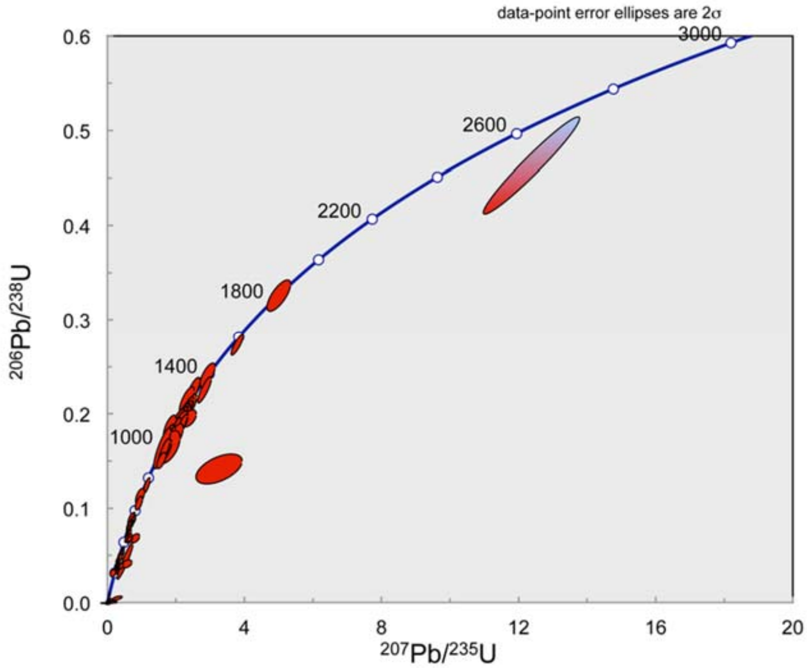

Fig. A.4 Concordia diagram showing 2σ ellipses of measured $^{206}Pb/^{238}U$ and $^{207}Pb/^{238}U$ ratios measured in detrital zircons from sample MOG-07.

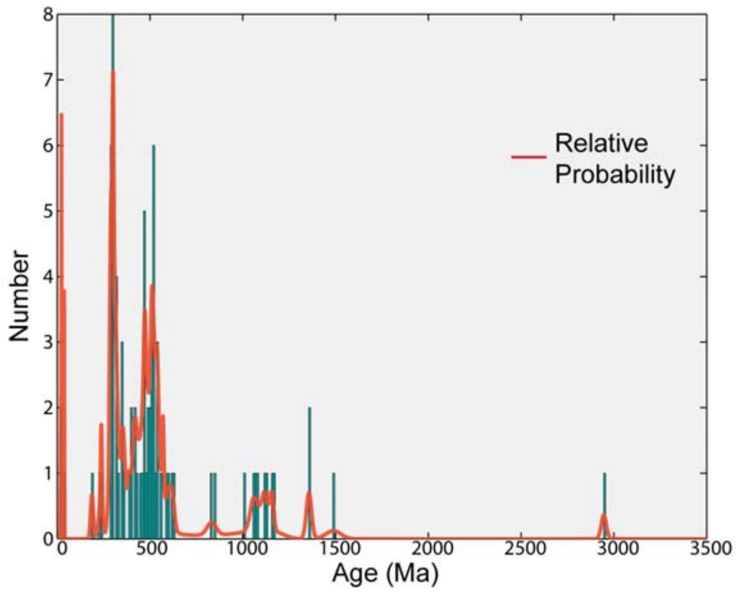

Fig. A.5 0-2.5 Ga results for HC-07 (7.1 Ma) detrital zircon sample from the Río Jáchal Fm., Foreland-N section.

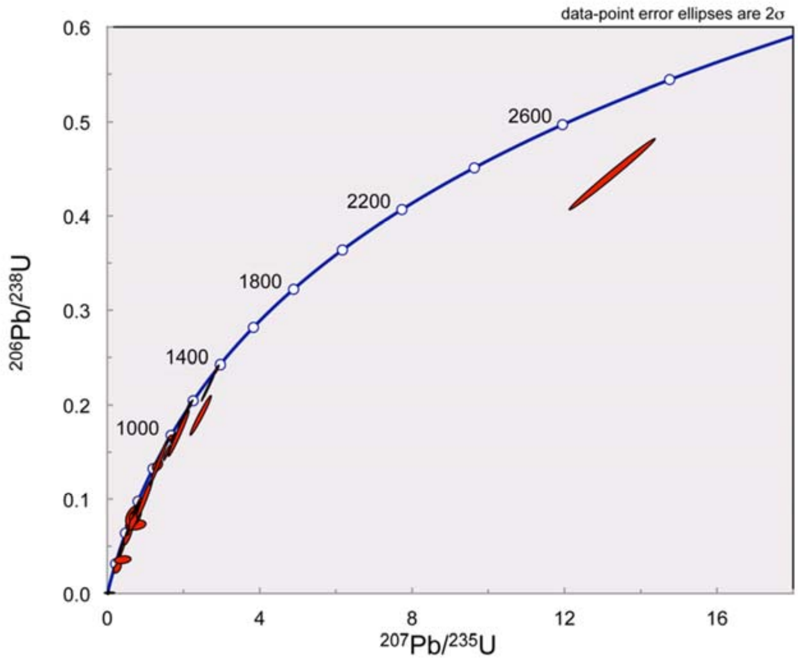

Fig. A.6 Concordia diagram showing 2σ ellipses of measured ^{206}Pb/^{238}U and ^{207}Pb/^{238}U ratios measured in detrital zircons from sample HC-07

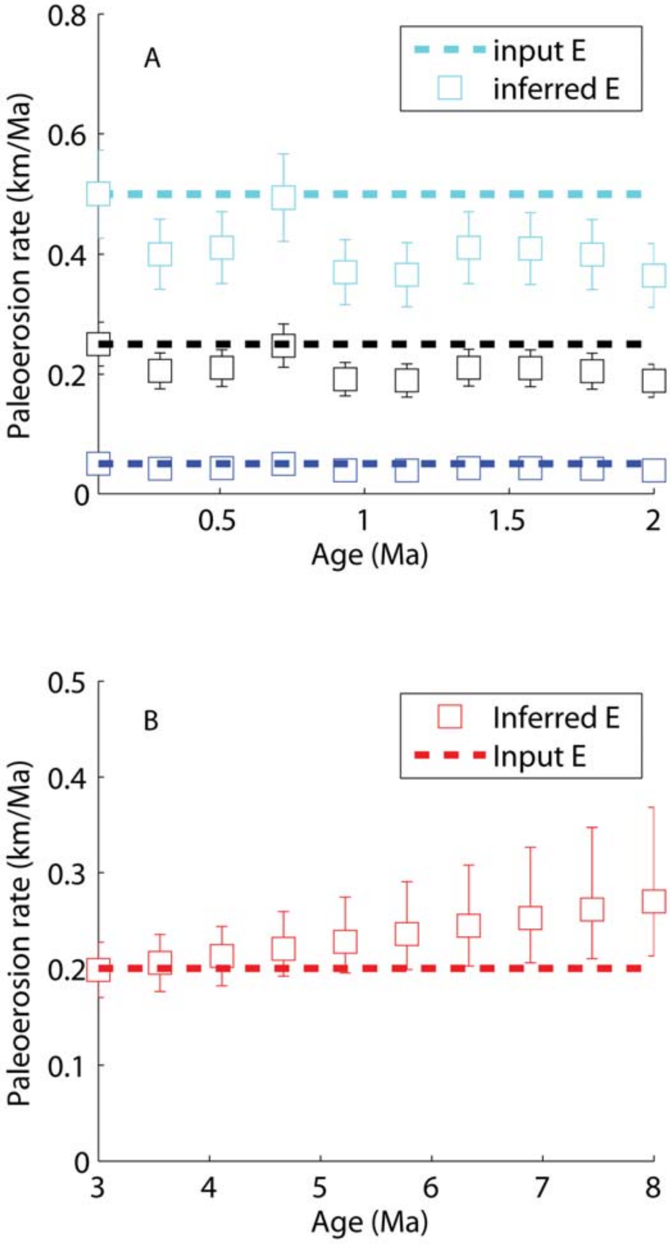

Fig. A.7 (A) Effects of ignoring changes in production rates due to secular variations in geomagnetic paleo-intensities for three different input paleo-erosion rates; (B) Effects of using the modern source-area elevation to calculate ^{10}Be paleo-erosion rates. Input E denotes the input paleo-erosion rate and inferred E denotes the inverted paleo-erosion rate signal.

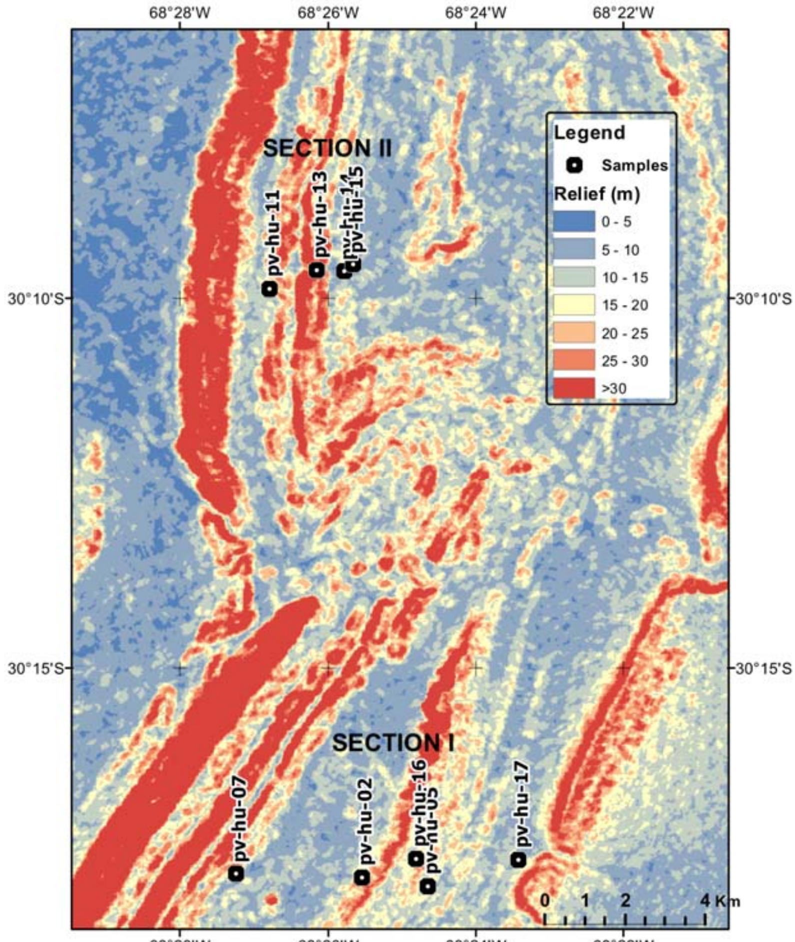

Fig. A.8: Relief map of the Foreland-N study area showing locations of samples. The relief was calculated within a 120 m radius using a 30 m resolution digital elevation model (1 arc-second SRTM Global Dataset - http://earthexplorer.usgs.gov).

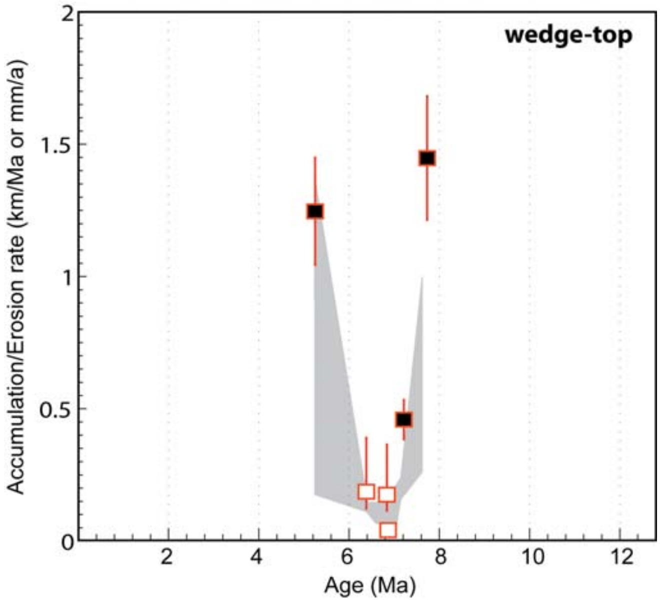

Fig. A.9: Paleo-erosion rate results for wedge-top samples if each sample remained 1 m beneath the surface of the deposit 100 ka prior to burial. Black-filled squares denote minimum possible paleo-erosion rate. Gray envelope shows no-hiatus results from the main text.

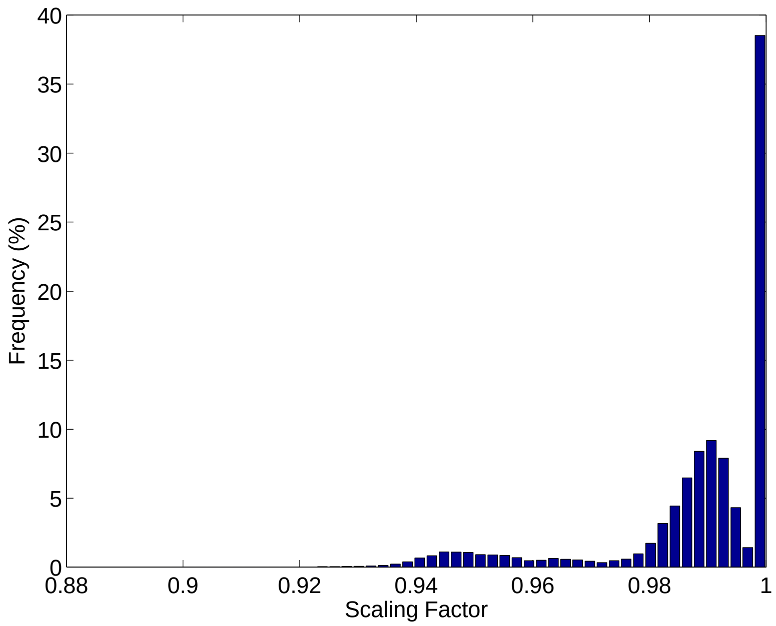

Fig. A.10: Histogram of scaling factors obtained pixel by pixel using a 90 m resolution SRTM DEM. Note that the majority of scaling factors is higher than 98%.